Earth-Science Reviews 139 (2014) 33–46

Contents lists available at ScienceDirect

Earth-Science Reviews

journal homepage: www.elsevier.com/locate/earscirev

Oceanic- and continental-type metamorphic terranes: Occurrence and exhumation mechanisms

Monica E. Erdman *, Cin-Ty A. Lee

Dept. of Earth Science, 6100 Main St. MS-126, Rice University, Houston, TX 77005, USA

ARTICLE INFO

Article history:
Received 25 April 2014
Accepted 22 August 2014
Available online 3 September 2014

Keywords:
High pressure
Ultrahigh pressure
Exhumation
Channel flow
Diapir
Buoyancy

ABSTRACT

Understanding the fate of subducted materials has important implications for the chemical and physical differentiation of the Earth, particularly the compositional evolution of the continental crust. Of interest here is how deeply-subducted materials return to the Earth's surface. We present a comprehensive global compilation of high-pressure, low-temperature metamorphic terranes for which peak metamorphic conditions have been constrained. These metamorphic terranes are classified based on tectonic setting: terranes in oceanic plate subduction zones were classified as oceanic-type and those in continent–continent collision zones were classified as continental-type. We show that oceanic-type terranes form under pressures less than ~2.7 GPa whereas continental-type terranes develop under greater pressure and slightly higher prograde geothermal gradients. Whereas these two terrane types probably share common descent paths (i.e. subduction), their separation in pressure–temperature space suggests that the mechanism and pathways of their exhumation likely differ. Here we present a simple buoyancy-driven model to explain the bifurcation of subducted material at depth and how exhumation regimes may change in different tectonic settings during the evolution of convergent margins. We explore two exhumation modes. In one, the hydrous nature of subducted sediments leads to a low-density, low-viscosity channel bounded by relatively rigid walls, thereby driving channel-like flow along the dipping slab surface. In the other mode, channel viscosity approaches that of the overlying mantle wedge, preventing channel flow but permitting vertical exhumation via diapirism. We show that the exhumation mode depends on slab dip and the viscosity ratio between the buoyant material and the overlying mantle (described by a dimensionless parameter, M). Due to a significant change in channel viscosity with the breakdown of hydrous minerals, we suggest that the transition in exhumation mode coincides with slab dehydration; at what depth this transition occurs depends on plate velocity and the initial thermal state of the slab. Such a model predicts channel flow to be limited to shallow depths and diapiric exhumation to greater depths, providing an internally consistent explanation for the apparent differences in peak metamorphic conditions of oceanic- and continental-type terranes if the former exhume via channel flow and the latter via diapirism. Because young, hot slabs dehydrate at shallower depths than old, cold slabs, the maximum depth to which channel flow can operate is greater in the latter. Finally, our model also predicts how the exhumation mode changes as the nature of subduction zones evolves during the closure of an ocean basin, beginning with oceanic plate subduction and culminating in continent–continent collision. In such a scenario, channel flow is favored during the subduction of dense, steeply dipping oceanic lithosphere, but a growing continental (low density) character to the subducted materials as the ocean basin closes should gradually shift the mode of exhumation to diapirism.

Contents

* Corresponding author.
E-mail addresses: mee5@rice.edu (M.E. Erdman), ctlee@rice.edu (C.-T.A. Lee).

http://dx.doi.org/10.1016/j.earscirev.2014.08.012
0012-8252/

1. Introduction

High-pressure metamorphic rocks exposed at the surface in subduction zones and orogenic belts are evidence that crustal materials are tectonically transported to and exhumed from great depths, in some cases exceeding ~150 km. Peak metamorphic assemblages typically indicate transport in very low (~7 °C/km) geothermal gradients (e.g. Liou et al., 2000), implying rapid advective transport during subduction. The presence of high-pressure mineral assemblages, such as coesite, requires exhumation from such depths at rates fast enough to inhibit complete retrogression of peak metamorphic assemblages (Chopin, 1984).

The mechanisms by which these deep-seated rocks are exhumed are unclear (cf. Hacker et al., 2013). A plethora of models have been proposed, including wedge extrusion of crustal material detached from the down-going plate (Ernst, 1975; Chemenda et al., 1995; Kylander-Clark et al., 2008), channel flow or ductile return flow along the down-going slab–mantle interface (Cloos, 1982; Burov et al., 2001; Gerya et al., 2002; Raimbourg et al., 2007; Warren et al., 2008; Beaumont et al., 2009; Horodyskyj et al., 2009), extensional–erosional collapse (Platt, 1993), and diapiric ascent of continental material (eg. Hall and Kincaid, 2001; Gerya et al., 2006; Currie et al., 2007; Behn et al., 2011; Little et al., 2011).

Of particular interest is whether terranes of different peak metamorphic conditions are formed and exhumed in different ways. Traditionally, these deep-seated metamorphic rocks have been respectively classified as "high-pressure" (HP) and "ultrahigh-pressure" (UHP) by the absence or presence of coesite, corresponding to ~2.7 GPa for this seemingly arbitrary divide. However, differences in protolith composition and tectonic setting have been suggested for HP and UHP rocks (Bally, 1981; Maruyama et al., 1996; Liou et al., 2004; Ernst, 2005), suggesting that more than just a phase transformation may distinguish these two groups. Here, we present a comprehensive global compilation of P–T data for HP and UHP terranes and confirm that terranes associated with oceanic subduction and continental subduction/collision indeed show distinctly different peak metamorphic conditions. Why are the P–T conditions of subducted materials so different between these two tectonic environments?

To explain the dichotomous fate of deeply-subducted materials, we develop simple scaling models, which show that subducted crustal materials can exhume via channel flow along the slab–mantle interface, exhume via diapiric ascent through the mantle wedge, or not exhume at all, depending on the viscosity of the subducted materials, slab dip and slab velocity. In particular, the viscosity of subducted materials is sensitive to the presence of hydrous phases and is therefore a quantity controlled by protolith composition and the thermal evolution of the subducting slab. Our models can be used to predict peak metamorphic conditions of exhumed terranes in different tectonic environments.

2. Global compilation of metamorphic conditions in HP and UHP terranes

2.1. Database and tectonic classifications

We compiled peak metamorphic conditions of worldwide high-pressure, low-temperature terranes (HP–LT) for which robust thermobarometry exists (Fig. 1). For a complete list of data and references see Table 1. Instead of classifying terranes based on the presence

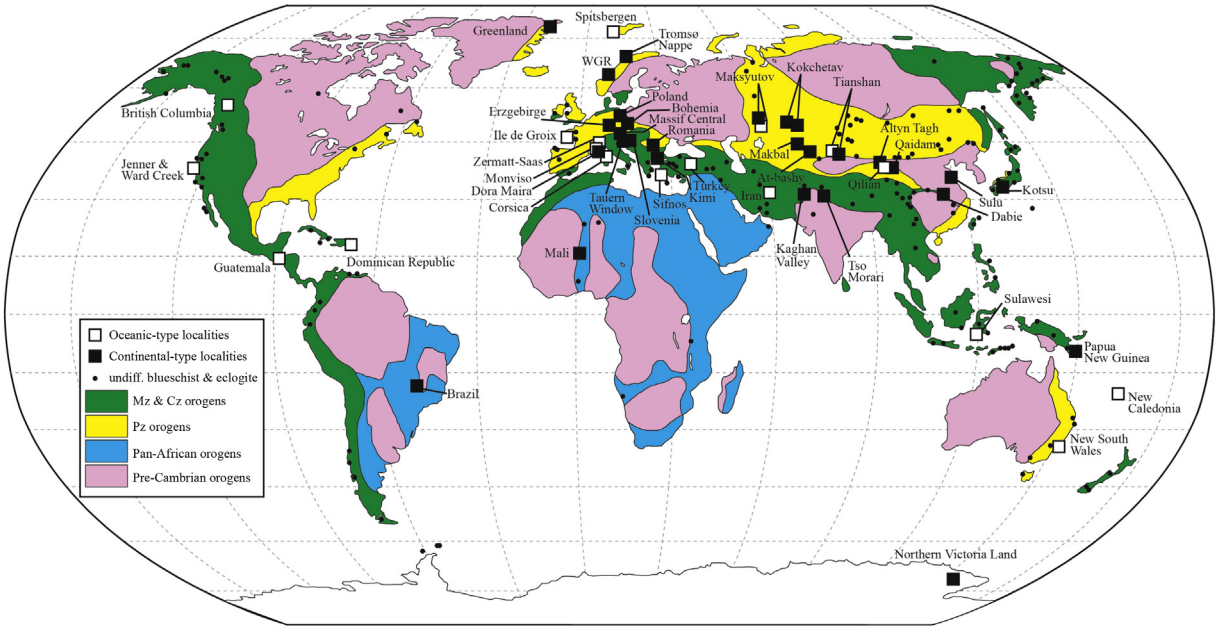

Fig. 1. Worldwide distribution of oceanic-type (open squares) and continental-type (black squares) metamorphic terranes for which peak metamorphic conditions have been well constrained (modified from Tsujimori et al., 2006). Small circles represent potential oceanic- or continental-type locations for which peak metamorphic conditions have not yet been constrained (Table S1; Maruyama et al., 1996).

or absence of coesite, we have chosen here to classify terranes based on tectonic environment. This allows us to evaluate whether there are fundamental differences in peak metamorphic conditions according to tectonic setting. To do so, we classify paleo-subduction zones as either *oceanic-type* or *continental-type*, according to the end-member classification scheme based on lithologic assemblages used by Song et al. (2006). This classification corresponds to the Pacific- and Alpine-type of Ernst (2005) and the B- and A-type defined by Maruyama et al. (1996), respectively.

Oceanic-type, as described by Ernst (2005), is here assigned to terranes formed in accretionary complexes. Accretionary complexes are typically associated with subduction of oceanic crust and typify much of the modern Pacific Rim. In such terranes, tectonized eclogitic or blueschist blocks or pods are typically associated within highly retrograded serpentinitic, metagraywacke, or schistose mélange. Protoliths include bedded cherts, basalts with MORB-like geochemical signatures, seamount fragments, ophiolites, reef limestones, graywackes, and trench turbidites. Oceanic-type trench terranes are also closely associated with slightly older or coeval calc-alkaline volcanic–plutonic terranes in a landward position.

Continental-type terranes are generally ascribed to continent–continent collisions and were identified here as follows (Ernst, 2005). Protoliths derive from continental basement complexes, overlying sediments, and volcanoclastics. In continental-type terranes, peak metamorphic conditions are primarily preserved in volumetrically minor eclogitic or garnet-pyroxenitic pods or slabs hosted within abundant orthogneiss or paragneiss. Continental-type complexes commonly extend hundreds of kilometers, comprise thin sheets sandwiched between lower-grade rocks bound by normal faults or migmatite zones, show (sub-) continental geochemical and petrologic characteristics, and contain post-collisional peraluminous granitic plutons. Calc-alkaline magmatic suites are scarce and S-type granitoids occur within the terrane itself instead of on the hanging-wall plate, as is the case of oceanic-type terranes (Ernst, 2005).

Data are gathered from the global compilations of Tsujimori et al. (2006), Brown (2007), and Tsujimori and Ernst (2014), as well as our own literature compilations. These include 47 locations worldwide (Fig. 1). The oldest includes the continental-type terranes of Brazil (Parkinson et al., 2001) and Mali (Caby, 1994; Jahn et al., 2001), which formed during the Pan-African orogenies of the Neoproterozoic. The only recognized HP terrane in Antarctica, exposed in the Lanterman Range of northern Victoria Land, formed in the early Paleozoic during the accretion of Gondwana (Palmeri et al., 2011). Also formed at this time is the oceanic-type Port Macquarie terrane in New South Wales, Australia (Och et al., 2003). Several terranes represent the Paleozoic Caledonide orogeny, including the oceanic-type terrane on the Norwegian island of Spitsbergen (Hirajima et al., 1988) and the continental-type terranes from northeastern Greenland (Gilotti and Krogh-Ravna, 2002) as well as the Western Gneiss Region (Cuthbert et al., 2000) and Tromsø Nappe (Corfu et al., 2003) of Norway. Across Europe, several continental-type terranes formed during the Paleozoic Variscan orogeny. These include the Bohemian Massif in the Czech Republic (Nakamura et al., 2004), the crystalline massif of Erzgebirge in Saxony, Germany (Massonne, 1999), the Leaota Massif of the South Carpathians in Romania (Săbău, 2000), the Massif Central in France (Lardeaux et al., 2001), and the Sudetes Mountains in southwestern Poland (Bakun-Czubarow, 1991, 1992). On the French Ile de Groix, an oceanic-type terrane comprises the contemporaneous Armorican Massif (Ballèvre et al., 2003; Bosse et al., 2005). The eastern continuation of the Variscan orogeny, known as the Central Asian Orogenic Belt, stretches from western Russia to central China. HP–LT terranes from this fold belt include the Maksyutov Complex of the southern Ural Mountains (Schulte and Sindern, 2002; Bostick et al., 2003), Kumdy-Kol and Kulet blocks of the Kokchetav Massif (Sobolev and Shatsky, 1990; Shatsky et al., 1995), At-bashy and Makbal locations in Kyrgyzstan (Tagiri et al., 1995), western Tianshan of northwest China (Zhang et al., 2007; Lü et al., 2008), southwest Altyn Tagh near Jianggalesayi, western China (Zhang et al., 2001), and the North Qilian and North Qaidam belts on the northern margin of the Tibetan Plateau, western China (Song et al., 2003, 2006; Zhang et al., 2009).

Younger terranes formed in Mesozoic–Cenozoic orogens are primarily found in the Alpine–Himalayan orogen, extending from Western Europe to Indonesia, and the Cordilleran orogen along the western coasts of North and South America. Terranes from the Alpine–Himalayan orogeny exposed in the Alps include the Zermatt–Saas Zone (Reinecke, 1991), Dora Maira Massif (Chopin, 1984), and the Monviso metaophiolite (Groppo and Castelli, 2010) in the western Alps and the Pohorje Mountains (Janák et al., 2004) and Tauern Window (Hoschek, 2001) of the eastern Alps. Alpine exposure extends south into the Schistes Lustré complex on the island of Corsica (Caron and Péquignot, 1986). HP–LT exposure continues eastward in Greece in the Kimi Complex of the Rhodope Mountains (Mposkos and Kostopoulos, 2001) and the island of Sifnos (Schmädicke and Will, 2003), in northwestern Turkey near the town of Orhaneli (Okay et al., 1998), and in the Sistan suture zone of Iran (Fotoohi Rad et al., 2005). The Kaghan Valley (O'Brien et al., 2001) and Tso Morari (Mukherjee and Sachan, 2001) terranes in Pakistan and India, respectively, comprise Himalayan exposures. In eastern China, the Dabie–Sulu terranes formed in the Triassic during the collision of the Sino-Korean and Yangtze cratons (Wang et al., 1989; Zhang et al., 1995). In the western Pacific, HP–LT terranes occur on the islands of Shikoku, Japan (Tsuchiya and Hirajima, 2013), Sulawesi, Indonesia (Parkinson et al., 1998), New Caledonia (Clarke et al., 1997), and the D'Entrecasteaux Islands of Papua New Guinea (Baldwin et al., 2008). In North America, oceanic-type terranes outcrop along the Cordilleran orogeny in British Columbia near Pinchi Lake (Ghent et al., 1993) and in the Franciscan Complex of California (Coleman and Lee, 1963; Ernst, 1993; Krogh-Ravna et al., 1994; Shibakusa and Maekawa, 1997). HP–LT terranes also occur along the South Motagua fault zone in Guatemala (Harlow et al., 2004) and on Samaná Peninsula in the Dominican Republic (Zack et al., 2004a).

In Fig. 1, we plot each of the locations discussed above on a world map along with its designated tectonic classification. Table 1 lists the age, peak metamorphic conditions, how these values were determined, rock type, associated orogeny (if known), and any references for each terrane. We also include the tectonic end-member classification as determined in this study. Supplementary Table 1 provides a list of additional blueschist and eclogite locations worldwide compiled from Maruyama et al. (1996). For many of these outcrops supplementary thermobarometric and/or age constraints are needed, though many have clear oceanic-type affinities (i.e. Klamath Mountains and California coast). We include the additional locations in Fig. 1 and Table S1 to acknowledge that our compilation (Table 1) is not exhaustive.

2.2. Constraints on peak metamorphic conditions

For blueschists and eclogites with relevant mineral assemblages in Table 1, peak metamorphic conditions are determined using the garnet–clinopyroxene–kyanite–phengite–coesite/quartz thermobarometer (Krogh-Ravna and Terry, 2004). Because the net transfer reactions employed in this thermobarometer are insensitive to Fe^{2+}/Fe^{3+} ratios, P–T conditions determined in this manner are considered robust (Hacker, 2006). Prior to development of the Krogh-Ravna and Terry (2004) thermobarometer, garnet–omphacite–phengite barometry provided pressure estimates for these mineral assemblages (Waters and Martin, 1993; Waters, 1996). Minimum pressure estimates for many continental-type terranes are determined by the presence, or former presence, of coesite or diamond. Additional methods used in the determination of peak pressure conditions in Table 1 include Al-in-opx (Harley and Green, 1982; Brey and Köhler, 1990), jadeite–albite–quartz barometry (Holland, 1980), phengite barometry (Massonne and Schreyer, 1989), Si content in phengite and biotite (Hermann, 2003), and garnet–kyanite–celadonite–muscovite–coesite thermobarometry in

Table 1
Compilation of global oceanic- and continental-type metamorphic terranes.

Location	Age (Ma)	Peak P (GPa)	Peak T (°C)	References	P determination	T determination	Age determination	Rock-type	Orogen	Type
Oceanic-type										
Pam Peninsula, New Caledonia	~40	1.6–1.9	~590	Tsujimori et al. (2006) (and references therein)	Gar–lws–cpx assemblage; THERMOCALC averages		U–Pb zircon	Lws-eclogite		Oceanic
Monviso, western Alps	45 ± 1	2.5–2.6	~550	Tsujimori and Ernst, (2014) (and references therein)	Lws pseudomorphs; gar–lws–cpx–phen–gln assemblage; THERMOCALC averages		U–Pb zircon	Lws-eclogite	Alpine–Himalayan	Oceanic
Sifnos, Greece	51	2	550–600	Brown (2007) (and references therein)	Jadeite barometry; phengite barometry	Fe–Mg exchange gar–cpx, gar–phen; lws stability	Ar–Ar in phengite	(Former) lws-eclogite, blueschist	Alpine–Himalayan	Oceanic
Zermatt–Saas Zone, western Alps	52 ± 18	2.6–3.0[a]	590–630	Brown (2007) (and references therein)	Coesite	Fe–Mg exchange gar–cpx	Sm–Nd in garnet	Eclogite	Alpine–Himalayan	Oceanic
Samaná Peninsula, Hispaniola (Dominican Republic)	84	1.6	360	Tsujimori et al. (2006) (and references therein)	Gar–cpx–ky–phen–qz/co thermobarometry	Fe–Mg exchange gar–cpx	Sm–Nd gl–WR isochron	Lws-eclogite		Oceanic
Sistan suture zone, Iran	~85	1.9–2.3	435–650	Bröcker et al. (2013); Brown (2007) (and references therein)	Gar–cpx–pg–gln–czo assemblage; THERMOCALC averages		Rb–Sr multiphase isochron	Eclogite, blueschist	Alpine–Himalayan	Oceanic
Schistes Lustré, Corsica	85	2	390	Tsujimori et al. (2006) (and references therein)	Gar–cpx–ky–qz/co thermobarometry	Fe–Mg exchange gar–cpx	Sm–Nd	Lws-eclogite	Alpine–Himalayan	Oceanic
Orhaneli, NW Turkey	~88	2.1–2.7	400–460	Brown (2007) (and references therein)	Jd + chld assemblage (min), no coesite (max)	Tc + lws assemblage	Ar–Ar in phengite	Lws-blueschist	Alpine–Himalayan	Oceanic
Kotsu area, eastern Shikoku, Japan	~90	2	600	Tsujimori and Ernst (2014) (and references therein); Endo et al. (2009)	Gar–cpx–phen barometry	Fe–Mg exchange gar–cpx	Lu–Hf multiphase isochron	Lws-eclogite		Oceanic
South Motagua fault zone (Carrizal Grande area), Guatemala	125–113	2.6	480	Tsujimori et al. (2006) (and references therein)	Gar–cpx–ky–phen–qz/co thermobarometry		Ar–Ar in phengite	Lws-eclogite	Cordilleran	Oceanic
Bantimala Complex, Sulawesi, Indonesia	~130–115	2.4–2.7	580–650	Brown (2007) (and references therein)	Gar–omph–phen barometry	Fe–Mg exchange gar–cpx	K–Ar in phengite	Lws-eclogite		Oceanic
Franciscan Complex, Jenner, CA, USA	~145	2.2	435	Brown (2007) (and references therein)	Gar–cpx–ky–phen–qz/co thermobarometry		Lu–Hf in garnet	Gln-eclogite	Cordilleran	Oceanic
Franciscan Complex, Ward Creek-Cazadero, CA, USA	~145	1.8–2.2	420–460	Tsujimori et al. (2006) (and references therein)	Gar–cpx–ky–phen–qz/co thermobarometry		Ar–Ar in phengite; Lu–Hf in garnet	Lws-eclogite	Cordilleran	Oceanic
Pinchi Lake, British Columbia, Canada	218–211	2.4–2.7	450	Ghent et al. (2009); Tsujimori et al. (2006) (and references therein)	Gar–cpx–ky–phen–qz/co thermobarometry	Fe–Mg exchange gar–cpx	K–Ar in phengite	Lws-eclogite		Oceanic
Maksyutov Complex, southern Urals (upper unit)	345–333	1.8–2.1	520–540	Brown (2007) (and references therein)	Lws pseudomorphs; lws + sph assemblage; THERMOCALC averages	Lws + gar + chl assemblage	Rb–Sr in all phases	Lws-rodingitized ultramafic rock	Central Asian Orogenic Belt	Oceanic
Western Tianshan, NW China	~350	2.5[a]	570–630	Zhang et al. (2007); Lü et al. (2008)	Gar–omph–phen barometry; coesite	Fe–Mg exchange gar–cpx	U–Pb in zircon	Eclogite	Central Asian Orogenic Belt	Oceanic
Ile de Groix, Armorican Massif, France	~370	1.8–2.0	450	Brown (2007) (and references therein)	Lws pseudomorphs; lws + gar + gln + ep assemblage; THERMOCALC averages		Rb–Sr, Ar–Ar in phengite	Lws-eclogite	Variscan	Oceanic
Motalafjella, Western Spitsbergen	475–450	1.7–2.4	575–645	Brown (2007) (and references therein)	Jadeite barometry; paragonite stability (max)	Fe–Mg exchange gar–cpx	Ar–Ar in phengite	Lws-eclogite	Caledonide	Oceanic
North Qilian Suture Zone, western China	464 ± 6	2.2–2.6	460–510	Song et al. (2006, 2007)	Gar–cpx–ky–phen–qz/co thermobarometry	Fe–Mg exchange gar–cpx	U–Pb zircon	Lws-eclogite	Central Asian Orogenic Belt	Oceanic
Port Macquarie, New South Wales, Australia	480–465	2.0–2.4	420–570	Tsujimori et al. (2006) (and references therein)	Gar–cpx–ky–phen–qz/co thermobarometry		Ar–Ar in phengite	Lws-eclogite	New England	Oceanic
Continental-type										
D'Entrecasteaux Islands, SE Papua New Guinea	8–2	2.8	700	Baldwin et al. (2008)	Gar–cpx–ky–phen–qz/co thermobarometry; coesite	Fe–Mg exchange gar–cpx; Ti-in-zrc; Ti-in-rut	U–Pb zircon	Eclogite		Continental
Tauern Window, eastern Alps, Austria	31.5	2.6	650	Hoschek (2007); Brown (2007) (and references therein)	Gar–cpx–ky–phen–qz/co thermobarometry		Rb–Sr multiphase isochron	Ky-eclogite	Alpine–Himalayan	Continental

Dora Maira Massif, Western Alps	35.4 ± 1	4.3	730	Brown (2007) (and references therein)	Coesite; Si content in phengite; ky + cel = coes + musc + gar		U–Pb in zircon	Whiteschist	Alpine–Himalayan	Continental
Kaghan Valley, Himalayas, Pakistan	46.2 ± 0.7	2.7–3.2	700–770	Brown (2007) (and references therein)	Gar–cpx–ky–phen–qz/co thermobarometry; coesite	Fe–Mg exchange gar–cpx	U–Pb in zircon	Eclogite	Alpine–Himalayan	Continental
Tso Morari Complex, Himalayas, India	53.5 ± 7	2.8[a]	700–800	Brown (2007) (and references therein)	Coesite	Fe–Mg exchange gar–cpx, gar–phen	U–Pb in zircon	Eclogite	Alpine–Himalayan	Continental
Pohorje Mountains, Eastern Alps, Slovenia	~90	3.0–3.1	760–825	Brown (2007) (and references therein)	Gar–cpx–ky–phen–qz/co thermobarometry; coesite pseudomorphs		U–Pb in zircon; Sm–Nd & Lu–Hf in garnet, omphacite	Eclogite	Alpine–Himalayan	Continental
Kimi, east Rhodope, northern Greece	>160	3.5[a]	750	Schmidt et al. (2010); Perraki et al. (2006); Bauer et al. (2007)	Diamond		U–Pb in zircon	Metapelite	Alpine–Himalayan	Continental
Su–Lu Terrane, Eastern China	~230	2.8[a]	725–850	Brown (2007) (and references therein)	Coesite	Estimated from phase assemblages included in zircons			Dabie–Sulu	Continental
Dabie Shan, Central China	~240	3.7	794	Brown (2007) (and references therein)	Gar–cpx–ky–phen–qz/co thermobarometry; coesite; diamond		U–Pb zircon, Sm–Nd (multiphase, WR)	Eclogite	Dabie–Sulu	Continental
At-bashy, Kyrgyzstan	~270	2.5[a]	660	Brown (2007) (and references therein)	Coesite		Rb–Sr multiphase isochron	Eclogite	Central Asian Orogenic Belt	Continental
Erzgebirge, Saxony, Germany	336 ± 2	4.5[a]	1000	Brown (2007) (and references therein)	Diamond		U–Pb zircon, monazite	Quartzofeldspathic gneiss	Variscan	Continental
Bohemian Massif, Czech Republic	340–355	4.5–4.9	1050–1150	Brown (2007) (and references therein)	Gar–cpx–ky–phen–qz/co thermobarometry	Fe–Mg exchange gar–cpx		Ky-eclogite	Variscan	Continental
Sudetes Mountains, SW Poland	355–340	3	700–800	Brown (2007) (and references therein)	Gar–cpx–ky–phen–qz/co thermobarometry; coesite		Sm–Nd WR	Eclogite	Variscan	Continental
Leaota Massif, South Carpathians, Romania	360–340	2.8–3.2	780–840	Brown (2007) (and references therein)	Gar–cpx–ky–phen–qz/co thermobarometry		Sm–Nd WR	Eclogite	Variscan	Continental
Northeast Greenland Caledonides	361–347	3.6	970	Brown (2007) (and references therein)	Gar–cpx–ky–phen–qz/co thermobarometry; coesite pseudomorphs		U–Pb zircon	Ky-eclogite	Caledonide	Continental
Massif Central, France	384 ± 16	2.8[a]	740–780	Brown (2007) (and references therein)	Coesite	Fe–Mg exchange gar–cpx		Eclogite	Variscan	Continental
Maksyutov Complex, southern Urals (lower unit)	388 ± 4	3.2[a]	650	Brown (2007) (and references therein)	Diamond		U–Pb zircon	Eclogite	Central Asian Orogenic Belt	Continental
Western Gneiss Region, Norway	405–400	2.8–3.5	640–730	Brown (2007) (and references therein)	Gar–cpx–ky–phen–qz/co thermobarometry; coesite		U–Pb zircon	Eclogite	Caledonide	Continental
Tromsø Nappe, Norway	452 ± 1.7	3.4	735	Brown (2007) (and references therein)	Gar–cpx–ky–phen–qz/co thermobarometry		U–Pb zircon	Eclogite	Caledonide	Continental
North Qaidam, western China	449–422	2.9–3.3	690–770	Mattinson et al. (2006); Brown (2007) (and references therein); Song et al. (2006)	gar–cpx–ky–phen–qz/co thermobarometry; coesite		U–Pb zircon	Eclogite	Central Asian Orogenic Belt	Continental
Makbal, Kyrgyzstan	~480	2.6[a]	610–680	Brown (2007) (and references therein)	Coesite	Fe–Mg exchange gar–cpx	K–Ar in paragonite	Quartz schist	Central Asian Orogenic Belt	Continental
Lanterman Range, Northern Victoria Land, Antarctica	~498–490	2.8–3.4	745–850	Palmeri et al. (2011) (and references therein)	Al-in-opx thermobarometry; coesite	Fe–Mg exchange gar, cpx, opx, ol; En-in-cpx, Ca-in-opx	Ar–Ar in barroisite	Eclogite, gar-bearing websterite	Ross	Continental
Jianggalesayi, southwest Altyn Tagh, west China	509–499	2.8–3.0	820–850	Brown (2007) (and references therein)	Gar–cpx–ky–phen–qz/co thermobarometry		U–Pb zircon	Eclogite	Central Asian Orogenic Belt	Continental
Kulet, Kokchetav Massif, northern Kazakhstan	514–502	2.7–3.5	560–720	Zhang et al. (2012); Brown (2007) (and references therein)	Gar–cpx–ky–phen–qz/co thermobarometry; Coesite		U–Pb monazite	Gar–ky-micaschists	Central Asian Orogenic Belt	Continental
Kumdy-Kol, Kokchetav Massif, northern Kazakhstan	~530	4.0–6.0[a]	920–1000	Brown (2007) (and references therein)	Diamond				Central Asian Orogenic Belt	Continental
Pan-African nappes of northern Mali, West Africa	~620	2.7[a]	700–750	Brown (2007) (and references therein)	Coesite	Fe–Mg exchange gar–cpx	Rb–Sr & Sm–Nd (multiphase, WR), Ar–Ar phengite	Eclogite	Pan-African	Continental
Pan-African nappes of Minas Gerais State, SE Brazil	~630	2.7[a]	800	Brown (2007) (and references therein)	Coesite			Granulite, orthogneiss, eclogite	Pan-African	Continental

[a] Indicates a minimum pressure.

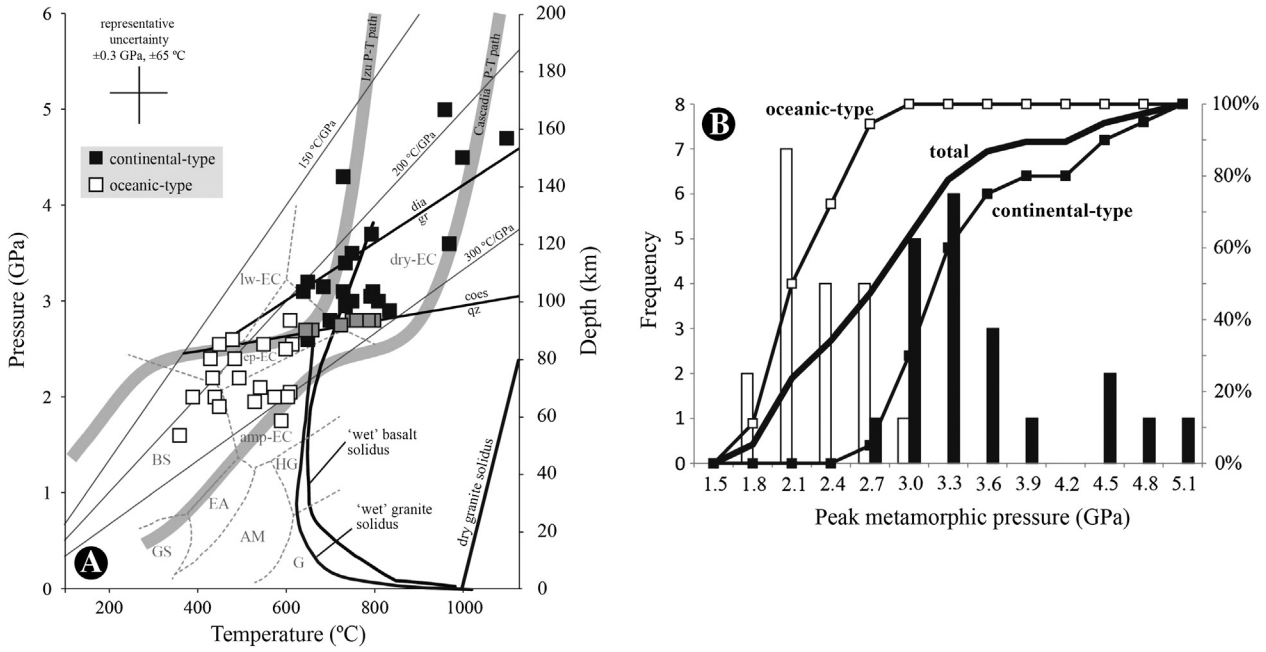

Fig. 2. (A) Peak metamorphic conditions of global oceanic-type (open squares) and continental-type (black squares) metamorphic terranes. Gray symbols denote minimum metamorphic conditions of continental-type terranes determined solely by the presence of coesite. P–T conditions compiled from Brown (2007) and Tsujimori et al. (2006), Tsujimori and Ernst (2014) and references therein; slab surface P–T paths from Syracuse et al. (2010); basalt H_2O-saturated solidus from Vielzeuf and Schmidt (2001); granite dry and H_2O-saturated solidi from Hermann (2003); metamorphic facies boundaries from Liou et al. (2004) [granulite (G), amphibolite (AM), epidote amphibolite (EA), greenschist (GS), blueschist (BS), high-pressure granulite (HG), and the subdivision of the eclogite facies into amphibole eclogite (amp-EC), epidote eclogite (ep-EC), lawsonite eclogite (lw-EC), and dry eclogite (dry EC)]. (B) Histogram and cumulative totals of peak metamorphic pressures. For a complete list of data, references, and explanations for the dataset presented in this figure, see Table 1.

pelites (Hermann, 2003). Paragonite stability provides a maximum pressure constraint (Holland, 1979) for the oceanic-type terrane from Sifnos, Greece; the jadeite + chloritoid assemblage provides a minimum pressure estimate (e.g. Guiraud et al., 1990) to oceanic-type rocks from Turkey. Paragonite or lawsonite stability with various phase assemblages allows for additional P–T constraints in combination with THERMOCALC averages (e.g. Schulte and Sindern, 2002; Ballèvre et al., 2003; Fitzherbert, 2003; Fotoohi Rad et al., 2005). Peak metamorphic temperatures determined independently from pressure for the terranes listed in Table 1 are calculated using Fe–Mg exchange thermometers (e.g. Ellis and Green, 1979; Green and Hellman, 1982; Harley, 1984; Krogh-Ravna, 2000). Other thermometers used include Ti-in-zircon (Watson and Harrison, 2005) and Ti-in-rutile (Zack et al., 2004b; Watson et al., 2006).

Peak metamorphic conditions plotted in Fig. 2a represent global data compiled for all recognized lawsonite-blueschist, lawsonite-eclogite, and UHP terranes. Oceanic- and continental-types form two distinct populations in P–T space (Fig. 2b): Oceanic-types metamorphosed at lower temperatures and pressure than continental-types. Nearly all continental-type terranes plot at pressures above the coesite–quartz transition and within the dry-eclogite field. Note, however, that two coesite-bearing terranes (Zermatt–Saas Zone of the western Alps and western Tianshan in NW China) classify as oceanic-type based on lithologic assemblage. In general, phase assemblages of continental-type terranes define slightly higher geothermal gradients than do oceanic-types. Hot and cold slab P–T paths from the Izu and Cascadia subduction zones (Syracuse et al., 2010) are plotted for comparison. Because the P–T conditions plotted in Fig. 2a are determined using a variety of methods, we assign a representative uncertainty of ±0.3 GPa and ±65 °C (Krogh-Ravna and Terry, 2004). The histogram in Fig. 2b excludes peak pressures for continental-type terranes defined solely by the presence of coesite (open symbols in Fig. 2a) because the presence of coesite only provides a minimum pressure estimate, thereby artificially shifting the data to lower pressures. It can be seen that almost all oceanic-type terranes are limited to pressures less than ~2.7 GPa (~80 km) whereas many continental-type rocks range from ~2.7 to 5.1 GPa (up to ~150 km).

3. The model

Any model that successfully describes the ascent of high pressure–low temperature rocks must explain the apparent dichotomy between the peak metamorphic pressures attained in oceanic-type and continental-type terranes. In other words, what prevents oceanic-type terranes from achieving peak metamorphic conditions greater than ~2.7 GPa? Here, we explore the role of compositional buoyancy in driving the ascent of deeply-subducted crust. Although there are other mechanisms for driving exhumation (see the Introduction section), almost all the high-pressure rocks in both terrane types are of low density or transported in a low-density matrix. Thus, it would seem that buoyancy must play some role in driving ascent. Indeed, numerical and analog experiments show the efficacy of buoyancy as an exhumation mechanism (e.g. Hall and Kincaid, 2001; Gerya et al., 2002; Beaumont et al., 2009; Behn et al., 2011). In this context, it has been proposed that oceanic-type terranes exhume along the sloping subduction channel at the slab–mantle interface (e.g. Ernst et al., 1997) and that vertical diapiric rise through the mantle wedge may be responsible for the ascent of continental-type terranes (e.g. Little et al., 2011), but why the ascent paths of subducted materials would be different in these two settings is unclear.

Here, we explore how the relative importance of these two end-member types of buoyancy-driven ascent mechanisms might change in different tectonic settings and during the evolution of a convergent margin. In so doing, our goal is not to reproduce geology in all its details with full-blown numerical models. Instead, our approach is to develop simple scalings that provide physical intuition on what controls the mode of ascent because, as far as we know, no such treatment has yet been presented. The goal of this paper is thus to enable the reader to make educated predictions so that targeted observations can be made. Our work lays the foundation for more detailed numerical modeling should the need arise.

We begin with buoyancy-driven channel flow along the top of the subducting slab as depicted schematically in Fig. 3. In this end-member, we assume that the channel material, made up of sediments

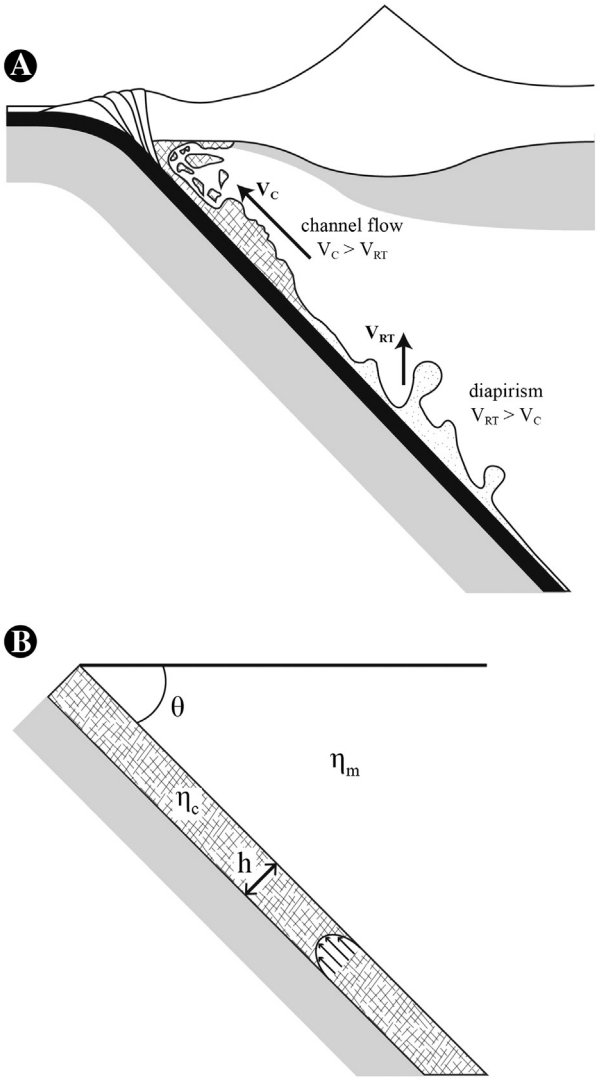

Fig. 3. (A) Schematic cross section illustrating the proposed model for flow of buoyant material in a subduction zone. We envision the subduction channel (cross hatched area) to consist of variably hydrated mantle, sediments, and fragments of oceanic crust. Diapirs (dotted area) likely comprise dehydrated sediments, crustal components, and partially molten continental crust and mantle. (B) Schematic cross section showing the simplified geometry of the subduction channel and parameters utilized in the model equations.

or hydrated peridotite (serpentinite), is of low density and of viscosity low enough compared to the overlying mantle wedge such that buoyancy-driven flow does not penetrate the mantle wedge but occurs along the dipping surface of the down-going plate. Additionally, we assume that the lower boundary of the subduction channel, comprising lithospheric mantle and portions of the subducting oceanic crust, is also highly viscous. We thus envision a low viscosity, low density sediment/serpentinite layer bounded by effectively rigid walls. A simple force balance (acceleration is zero) with no slip along the walls shows that the flow velocity V_C scales as:

$$V_C \approx \frac{\Delta\rho g h^2 \sin\theta}{\eta_c} \tag{1}$$

where $\Delta\rho$ is the density difference between the channel material and the surrounding mantle (kg/m^3), g is the gravitational acceleration, h is the channel thickness (m), η_c is the dynamic viscosity of the buoyant material (Pa·s), and $\sin\theta$ accounts for the slab dip. This approach is similar to that taken by Guillot et al. (2001), Raimbourg et al. (2007) and Horodyskyj et al. (2009). We have assumed a Newtonian viscosity for simplicity. Eq. (1) is essentially that of the Poiseuille flow with the constants dropped because we are interested in orders-of-magnitude. Ascent is favored when channel density is low and viscous resistance is low. Thus, exhumation velocity increases with the square of the channel thickness and inversely with viscosity. Channel flow velocities decrease with decreasing channel dip.

If, instead, the viscosity is too high to ascend via channel flow, diapiric rise into the overlying mantle wedge might occur (i.e. the development of a Rayleigh–Taylor instability). Such a situation might occur as hydrous minerals in the subducted materials breakdown and are expelled during prograde metamorphism, causing the channel viscosity to increase significantly. As an end-member scenario, we envision chemically buoyant bodies of dry sediments/continental crust to develop into diapirs at the slab–mantle interface when the viscosity of the channel approaches that of the overlying mantle wedge. The rate of ascent of a diapir, based on a force balance of a rising buoyant sphere, should scale as:

$$V_{RT} \approx \frac{\Delta\rho g h^2}{\eta_m} \tag{2}$$

where η_m is the mantle viscosity (or simply the viscosity of the overlying material) and h is the diapir radius, which we take to scale with the channel thickness. Here, we have assumed that $\eta_m > \eta_c$, that is, the resistance to flow is governed by the mantle wedge and not by internal deformation within the channel or diapir. In detail, the diapiric ascent of the buoyant material is governed by the physics of how Rayleigh–Taylor instabilities grow. There is a characteristic wavelength of perturbation that grows the fastest. This characteristic wavelength scales with h, leading to a growth rate that follows the same scaling as in Eq. (2) (Conrad and Molnar, 1997). We note that Eq. (2) is only valid for Newtonian viscosities and where $\eta_m > \eta_c$. As η_c approaches or exceeds η_m (or, equally, as η_m approaches η_c), the above relationship breaks down. It seems unlikely that the dehydration of sediments and serpentinites would cause the channel viscosity to exceed that of nominally anhydrous mantle. However, water weakening of the overlying mantle may cause η_m to decrease and approach η_c. Diapiric ascent is facilitated by low diapir density and low viscous resistance and therefore scales with the square of the diapir radius and inversely with mantle viscosity.

Regardless of the exhumation mode, for buoyant material to exhume, flow must overcome the downward drag of the subducting slab (Fig. 4). We therefore introduce two dimensionless parameters to describe the fate of subducted material:

$$C = {V_C}\Big/{V_P} \tag{3a}$$

$$D = {V_{RT}}\Big/{V_P \sin\theta}. \tag{3b}$$

When C (C for channel flow) is high, buoyant material exhumes via channel flow, and likewise, for high D values, diapiric ascent rates exceed the vertical subduction component so material rises (D for diapir). When C or D is less than unity, buoyancy-driven ascent is slower than the downward plate velocity, so sediments or crust continues to subduct.

The boundary between the two ascent regimes in Fig. 4 thus determines the exhumation mode of buoyant material. We define this boundary to be M, for exhumation mode, which occurs when $C = D$, or more specifically, when the vertical diapiric velocity V_{RT} is equal to the vertical component of the channel velocity, i.e., $V_C \sin\theta$:

$$M = \frac{V_{RT}}{V_C \sin\theta} \approx \frac{\eta_c}{\eta_m \sin^2\theta}. \tag{4}$$

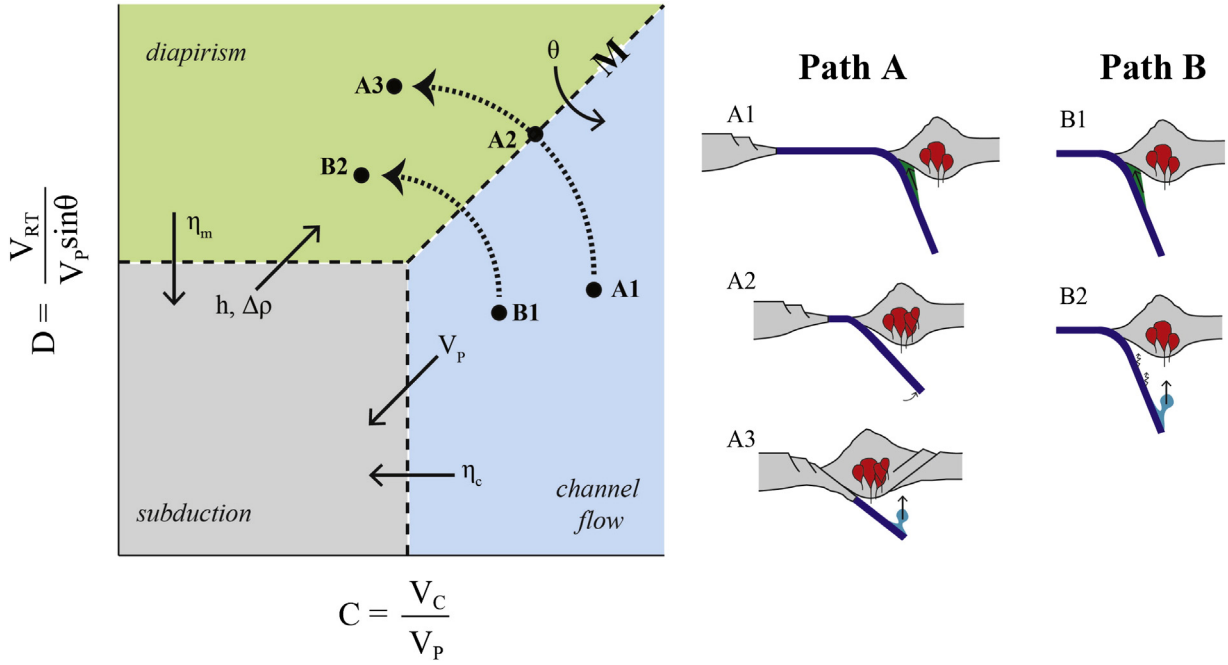

Fig. 4. Schematic plot of the dimensionless parameters C versus D. Transitions between the subduction, channel flow, and diapirism regimes are shown by the thin, dashed lines. The small, solid arrows demonstrate the effect of increasing various parameters. The boundary labeled *M* is defined by Eq. (4). Thick, dashed arrows represent scenarios that may result in an exhumation regime shift. Path A depicts changes expected during the closure of an ocean basin: oceanic lithosphere subduction (A1), encroachment of a continental margin (A2), and continent–continent collision (A3). Path B represents changes expected along the slab–mantle interface: at shallow depths subducted materials are hydrous and have low viscosity (B1) whereas prograde metamorphism leads to dehydration and an increased viscosity at depth (B2).

When *M* approaches or exceeds 1, material rises diapirically and when $M < 1$, material rises via channel flow. Based on Eq. (4), it can be seen that ascent mode is determined by the subduction angle and the viscosity contrast between the buoyant and overlying material, i.e., η_c/η_m. Clearly, if the slab dip approaches zero, the only mode of ascent is via diapiric rise because the pressure gradients along the slab interface are too low. Likewise, when slab dip is high, channel flow is favored. For a given slab dip, if channel viscosity is very low compared to the mantle viscosity, channel flow will dominate. As channel viscosity approaches that of the mantle, diapiric rise will be favored and channel flow will cease. Eq. (4) also shows that the thickness *h* of the low-density channel does not control ascent mode. Thickness of the channel *h* controls only the timescales of ascent via channel or diapiric flow.

The dependency of *M* on viscosity contrast has important implications because factors that may affect the viscosity contrast include temperature, partial melting, dehydration of the exhuming material, and subsequent hydration or addition of other volatiles to the overlying mantle. These factors are likely to vary in different tectonic environments and may also change dynamically during the descent of subducted materials into the mantle. In the Discussion section, we will explore these effects in more detail.

4. Discussion

4.1. Model parameters

Using the model described above, we seek to answer several questions. First, what conditions permit exhumation? To answer this question requires investigating likely values for the parameters invoked in Eqs. (1) and (2), which demonstrate that exhumation velocities of buoyant material not only depend most strongly on the characteristic length scale of the channel material and the viscosity of the channel, but also vary with density difference, and, in the case of channel flow, slab dip. Fig. 5 plots velocity calculations for each exhumation mode, demonstrating the effect of *h* and viscosity. Because instabilities grow while attached to the slab, their growth rate must exceed the downward plate velocity in order to develop. Diapir velocities therefore do not converge at the origin as is the case for channel flow velocities. The velocities plotted in Fig. 5 are approximate values calculated using the scalar relationships in Eqs. (1) and (2).

The length scale in the channel flow regime is equivalent to the thickness of the channel. In the case of diapirism, we make the simplifying assumption that the detachment of buoyant material is in the form of a spherical diapir, and thus the length scale refers to the radius of that sphere. In both exhumation regimes, we envision that the length scale varies with trench sediment supply, subduction erosion, and the efficiency of continental or arc subduction in the case of continental collision. Trench sediment supply thickness varies globally from 0.3 to 8.0 km (Clift and Vannucchi, 2004; Heuret et al., 2012). We posit that the length scale is similar to this range and probably does not exceed the thickness of the subducting crust. That velocity scales with h^2 predicts that flow is slowest in thin channels and increases rapidly as *h* increases. For example, material rising in a 1 km-thick channel travels up dip at <1 cm/yr whereas in a 4 km-thick channel velocities reach ~8 cm/yr (for a constant channel viscosity of 10^{19} Pa·s; Fig. 5a). These velocity estimates are comparable to plate tectonic rates.

Viscous forces are important because viscosity can vary by orders of magnitude. Constraints on mantle viscosity are primarily estimated from post-glacial rebound studies (e.g. Bills et al., 1993; Mitrovica, 1996). Estimates from experimental studies suggest that the asthenosphere has a viscosity on the order of 10^{18}–10^{19} Pa·s (Hirth and Kohlstedt, 1996), though dehydration of the subducting slab and fluid flux into the mantle wedge may decrease this value (Hirth and Kohlstedt, 2003). Viscosity in the subduction channel is on the order of ~10^{17} Pa·s (e.g. Shreve and Cloos, 1986), and varies significantly with dehydration. The primary factors that affect mantle wedge and channel viscosities are presumed to be temperature, volatile content, and degree of partial melting. Given these uncertainties, we make calculations for several rheological conditions (Fig. 5). Due to the inverse relationship between flow velocity and η in Eqs. (1) and (2), high viscosity decreases exhumation rate. For a constant channel

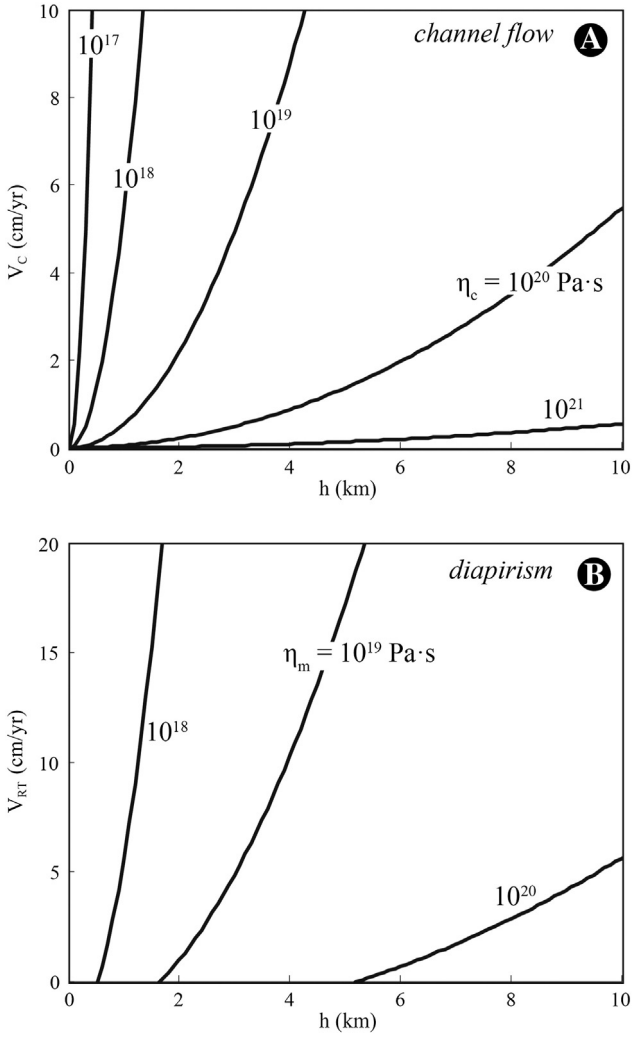

Fig. 5. (A) Up-dip channel flow and (B) vertical diapir velocities calculated for several viscosities with $\Delta\rho = 250$ kg/m^3, $\theta = 45°$, and $V_P = 3$ cm/yr.

thickness of 4 km, channel flow occurs at ~8 cm/yr when the channel viscosity is 10^{19} Pa·s, ~1 cm/yr when channel viscosity is 10^{20} Pa·s, and nearly zero when channel viscosity is 10^{21} Pa·s. Such order-of-magnitude increases in channel viscosity can act to suppress exhumation via channel flow. Similarly, high mantle viscosity acts to inhibit diapir formation. For a diapir with a 4 km radius, diapiric ascent reaches rates of 10 cm/yr when the mantle viscosity is 10^{19} Pa·s, but stops when the mantle viscosity increases to 10^{20} Pa·s.

As the driving mechanism of this model, buoyancy depends on the density difference between the exhuming material and the mantle. Exhumation will only occur if buoyancy forces are positive (i.e. $\Delta\rho$ is greater than zero). In comparison to mantle peridotite (~3300 kg/m^3) at 1.4 GPa and standard temperature (Carlson, 2001), some possible low-density lithologies in subduction zones include metasediments, such as metagraywacke (2670 kg/m^3), phyllite (2780 kg/m^3), and calcite marble (2760 kg/m^3), gneiss (2720–2800 kg/m^3), felsic granulite (2800 kg/m^3), serpentinite (2600 kg/m^3), and andesite (2650 kg/m^3). Due to the lithologies involved, $\Delta\rho$ is likely less than 700 kg/m^3. We use $\Delta\rho = 250$ kg/m^3 for our velocity calculations, based on UHP metapelite density calculations at high pressure (Behn et al., 2011). This value is expected to change with compositional variability, and likely decreases with depth as minerals transform to their high-density polymorphs. An increase in the density difference causes buoyancy forces to increase slightly. Increasing $\Delta\rho$ by 100 kg/m^3 increases velocities by ~0.2 cm/yr.

Slab dip additionally affects channel flow. For gentle slopes, buoyancy forces are low in the up-dip direction; at steep slopes, up-dip velocities increase. Because slab dip varies from ~20 to 65° among subduction zones today (e.g. Wada and Wang, 2009), it is likely that exhumation velocities vary between global subduction zones as well as through time at a single site due to the effect of subduction angle. A decrease in slab dip from 60° to 30° reduces exhumation velocities by ~0.3 cm/yr. Though this change is small, the effect may be large in combination with viscosity variability due to prograde metamorphism.

Table 2 defines possible values for each of the parameters discussed above and their references. Many of these variables can vary significantly on Earth. This study attempts to capture the likely variation in expected exhumation conditions given the uncertainties and demonstrated variation in parameter values. We present this model to provide an intuitive understanding of exhumation in convergent zones, not as a wholesale consideration of all possible parameter combinations.

4.2. Predicting the exhumation regime transition

A second goal of this study is to determine what conditions favor formation of oceanic-type versus continental-type metamorphic terranes. We ask, when might buoyant material transition from exhuming in a channel flow regime to a diapirism regime? As discussed above, the boundary between the two regimes in C–D space is defined by the parameter M in Eq. (4), which shows that exhumation mode depends on slab dip and viscosity contrast η_c/η_m (Fig. 4).

When examining the effect of slab dip, it is useful to consider extreme cases. Under flat slab conditions, when $\theta = 0°$, the pressure gradient goes to zero within the subduction channel and the buoyancy force acts in the vertical direction. Consequently, M approaches infinity and buoyant material may only exhume diapirically, if at all. When subduction is near vertical, however, the subduction angle term is neglected and the exhumation mode depends solely on the viscosity contrast. In this case channel flow is indistinguishable from diapirism, as both occur along the same vertical pathway. Thus, shallow dips favor diapirism and steep angles favor channel flow. We may now consider the effect of the subduction angle on the transition from oceanic to continental subduction during orogeny. During oceanic plate subduction, slab-pull forces are strong, and dense oceanic lithosphere subducts fast. In this case, buoyant materials supplied to the trench are limited to oceanic sediments. This

Table 2
Parameter values.

Parameter	Definition	Values	Reference
θ	Subduction angle	20–65°	Wada and Wang (2009)
V_P	Plate velocity	3–8 cm/yr	Wada and Wang (2009)
h	Channel thickness/diapir radius	0.3–10 km	Heuret et al. (2012); Clift and Vannucchi (2004)
η_c	Channel viscosity	10^{16}–10^{20} Pa·s	Shreve and Cloos (1986)
η_m	Mantle viscosity	10^{18}–10^{20} Pa·s	Hirth and Kohlstedt (1996, 2003)
$\Delta\rho$	Density difference at 1–3 GPa	0–650 kg/m^3	Behn et al. (2011)
τ_{dehy}	Dehydration at 2 kbar	650–750 °C	Huang and Wyllie (1973); Schmidt and Poli (1998); Bromiley and Pawley (2003); Schmidt et al. (2004)

situation may continue until more buoyant crust enters the trench—in the form of a micro-continent, oceanic plateau, or continental margin. As subduction of continental lithosphere begins and the plate boundary evolves into a continental collision zone, subduction slows, and the subduction angle may shallow due to the decreasing negative buoyancy. Thus, we expect exhumation of buoyant material to transition from channel flow during oceanic subduction to that of diapirism during mature stages of continental collision. The evolution from oceanic to continental subduction may thus mark a transitional time for exhumation processes, as subduction angles change and the amount of low-density, dry, felsic material entering the subduction zone increases. This concept was first conceived to reconcile the differences between small and large UHP terranes (Kylander-Clark et al., 2012), but may be expanded to consider oceanic-type terranes.

Because viscosity can vary by several orders of magnitude, we suggest that the viscosity ratio may also play an important role in determining exhumation mode. When $\eta_m > \eta_c$ and $M < 1$, channel flow acts as the dominant exhumation mode. This situation is favored by low internal viscosity—enhanced by high water contents and a high flux of sediment. As channel material dehydrates, a hydration front may move upward into the mantle wedge, in the form of serpentinized peridotite (e.g. Gerya et al., 2002). This process may widen the channel, increasing the exhumation rate by means of channel flow. As dehydration continues, however, the viscosity (and density) of the channel material will begin to rise, increasing the resistance to the buoyancy force. Thus, dehydration will eventually cause η_c to approach η_m and, subsequently, their ratio to approach unity. This situation leads to a transition from channel flow exhumation to diapiric exhumation.

We estimate when this transition occurs by modeling heat diffusion into a slab to determine the onset of dehydration. If the timescales for the slab to reach dehydration temperatures are known, the depth at which the transition occurs can be determined from the subduction rate and geometry. In the example shown in Fig. 6, we calculate 1-D heat diffusion into a 50 Ma lithospheric slab inserted into a hot mantle with a constant far-field temperature (this was done by assuming a constant temperature at distances much farther than the characteristic diffusion length scale of interest). The slab's initial thermal state is assumed to represent that of a growing thermal boundary layer, which is conventionally modeled by conductive cooling of an infinite half-space beginning with a vertically uniform mantle of 1400 °C (Eq. 4-113, Turcotte and Schubert, 2002). The slab is then injected into a uniformly hot mantle and allowed to heat up, approximating subduction. Heat diffusion into the slab is calculated by solving the partial differential equation in MATLAB with a thermal diffusivity of 10^{-6} m^2/s. The colored lines in Fig. 6a plot the temperature profiles for several time steps. Considering the top 10 km of this slab to represent the subducted crust, we plot temperature changes through time for this depth interval within the slab (Fig. 6b).

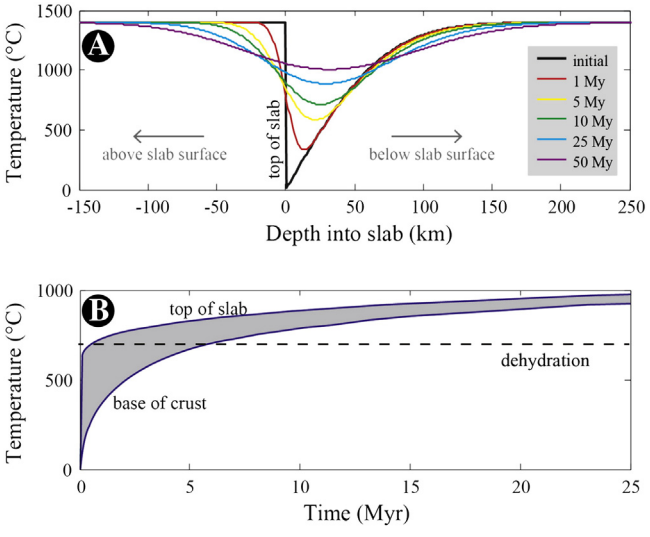

Fig. 6. (A) Cross-sectional 1-D temperature profiles achieved after 1, 5, 10, 25, and 50 My of heat diffusion. The thick black line shows the initial temperature profile calculated for 50 Ma lithosphere. Left and right boundaries are fixed at 1400 °C at a significant distance from the slab surface. Positive x-axis distance values represent the depth into the slab; negative distances are above the slab surface. (B) 1-D heat diffusion profiles through time for the top 10 km of the slab (shaded region). Dashed line approximates dehydration reactions at 700 °C. (For interpretation of the references to color in this figure, the reader is referred to the web version of this article.)

If we consider the transition from channel flow to diapiric exhumation to be primarily controlled by viscosity, and dehydration the chief control on viscosity, we can estimate the time it takes for dehydration to occur from calculations of heat diffusion. Dehydration of a heterogeneous lithologic terrane occurs over a spectrum of temperatures (Hacker et al., 2003). Due to this expected variability, we consider several relevant dehydration reactions to approximate complete devolatilization for a range of crustal compositions. In muscovite-bearing granitic compositions, muscovite dehydration occurs at ~750 °C at 2.0 GPa (Huang and Wyllie, 1973). The water-saturated basalt solidus occurs at 700 °C at 2.0 GPa (Schmidt and Poli, 1998). In water-saturated pelitic compositions, melting begins at ~650 °C at similar pressures (Schmidt et al., 2004). Additionally, serpentinite breakdown occurs at ~675 °C at 2.0 GPa (Bromiley and Pawley, 2003). Because these dehydration temperatures are similar, we use ~700 °C as a generalized dehydration temperature to account for the wide compositional variation in subducted materials. The characteristic time required for the slab to dehydrate is given by:

$$\tau_{700} = ah^2/\kappa \tag{5}$$

where κ is the thermal diffusivity (10^{-6} m^2/s) and a is a constant obtained from the numerical solutions of the heat diffusion equation and depends on the slab's initial thermal state, including slab age and slab thickness. Fig. 7 shows how the dehydration time scale changes with depth into the slab. Not surprisingly, dehydration occurs quickly (<1 to 3 Ma) in hot, young slabs and slowly (up to 10 Ma) in cool, old slabs. For hot, young slabs, this implies that dehydration of the top 10 km of the slab (i.e. the oceanic crust) will occur at vertical subduction depths of 40–70 km and for cold, old slabs dehydration will occur at depths of 150–200 km in the mantle, assuming a subduction rate of 3 cm/yr and 45° slab dip. Thus, where young lithosphere subducts, channel flow may be limited to shallow depths. Where old lithosphere subducts, we predict that channel flow may extend to greater depths.

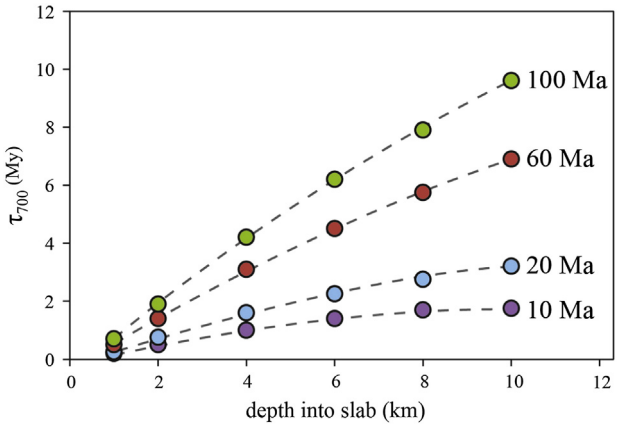

Fig. 7. Plot of the characteristic time it takes to reach 700 °C via heat diffusion (τ_{700}) versus depth into the slab. Variation with lithosphere age is given by the dashed lines. Young, hot lithosphere heats up quicker than old, cold lithosphere.

This also implies that diapirism would commence earlier where young lithosphere subducts.

We now return to the discussion of an evolving convergent margin to place it in the context of dynamically changing subduction angles and viscosity contrasts. Transition paths discussed below are depicted schematically in Fig. 4 (paths A and B). In the early stages of ocean basin closure, subduction of oceanic lithosphere results in strong slab-pull forces and fast subduction velocities. Inputs to the trench include hydrous oceanic sediments and hydrothermally-altered oceanic crust. In such tectonic settings we may expect low channel viscosity – and thus a low viscosity contrast – which favors channel flow as the mode of ascent for buoyant material (spot A1 in Fig. 4). Upon encroachment of a micro-continent or continental margin to the trench, subduction of compositionally buoyant continental crust increases. Such material may include terrigenous sediments and continental basement complexes, the latter of which may be less hydrated compared to oceanic sediments and altered oceanic crust. The increased amounts of dry and buoyant material supplied to the trench may shallow the subduction angle, increase the viscosity contrast, and slow subduction (A2). The slowing of subduction may also increase the thermal gradient (e.g., dT/dP) during descent, consistent with the slightly higher temperatures seen in continental-type eclogites. Due to these changes, we expect buoyancy-driven exhumation to shift to diapirism during the final closure of an ocean basin (A3). We might also predict diapirism to prevail if an arc or oceanic plateau collides with a trench. It has been suggested that an oceanic plateau collided with western North America around ~85 Ma (Saleeby, 2003) and may be associated with the formation of the Pelona–Orocopia–Rand schist in California. Although continental-type rocks have not yet been found in the schist locality, our analysis suggests that underplated sediments might exist beneath southwestern USA. In the context of this model, it is not impossible that both oceanic- and continental-type terranes may form in the same orogen (e.g. Song et al., 2006). Our analysis predicts that the two will be separated in time and space, with the continental-type terrane slightly younger and located further inboard of the trench than the oceanic-type terrane. However, subsequent removal of either terrane via subduction erosion, deformation, or incomplete exhumation may preclude outcrops of both terrane types in the field.

Finally, in addition to changes through time during the evolution of a convergent margin, the viscosity contrast may change within the subducting slab itself. Prograde metamorphism dehydrates subducting sediments and crust, leading to an increase in viscosity contrast at depth and, hence, a transition from channel flow (B1) to diapiric exhumation (B2) along the slab–mantle interface. Thus, even in oceanic subduction zones where we would expect to see some materials being exhumed by channel flow into the forearc, we might also predict some materials to rise diapirically. However, any diapiric rise of sediments would occur further down the slab, depending on when dehydration occurs and how long it takes for the diapir to develop and separate from the slab. For example, consider a 6-km-thick hydrated layer on a 50 Ma oceanic lithosphere subducting at 3 cm/yr with a 45° dip. The top 6 km will dehydrate in ~4 Ma ($\tau_{700} = 4$ Ma), at which point the slab will have descended a vertical distance of ~85 km. This is the depth at which channel flow ceases and exhumation transitions to diapirism. There is, however, a finite time for a diapir to separate from the down-going slab, causing exhumation to delay to greater depths. We estimate this time by dividing the layer thickness by the diapir ascent velocity, yielding a delay time of ~1 Myr (ascent velocity is ~0.6 cm/yr assuming a radius of 6 km and $\eta_m = 10^{20}$ Pa·s; Fig. 5). Incorporating this delay time, we estimate the diapir separates from the slab at a vertical depth of ~105 km (20 km deeper than the onset of dehydration) and ~75 km inboard of the trench. Consequently, we predict that any underplating in oceanic subduction zones would occur well inboard of the trench and may not appear intimately linked to the fore-arc in the geologic record.

4.3. The fate of ascending diapirs

Finally, an important question to address is whether ascending diapirs will melt. Recently, it has been suggested that rising diapirs may accrete at the bottom of the over-riding plate, which if true, would imply that continental crust could grow from below by relamination of sediments (Hacker et al., 2011). These authors suggest that buoyancy-driven differentiation during subduction causes mafic rocks to subduct and felsic rocks to ascend. A potential problem with this hypothesis is that relaminated sediments would be expected to have high K, U and Th contents, resulting in high radiogenic heat production in the lower crust, which seems unlikely given the current understanding of the distribution and abundance of heat producing elements in the continental crust (Rudnick and Gao, 2003). Hacker et al. (2011) suggested that these rising diapirs might partially melt, and if such melts were extracted into the mid- or upper-crust, the remaining solid residues (restites) at the base of the crust would be depleted in heat-producing elements. Indeed, many continental-type terranes contain abundant leucosomes or granitoid plutons, suggesting that melting occurred during exhumation (e.g. Hill et al., 1995; Song et al., 2014). In addition, deep-seated metasedimentary xenoliths in collisional orogens appear to be restitic (Behn et al., 2011). Determining whether melting occurs upon diapiric exhumation through the mantle is thus important.

We approach this problem by modeling the thermal evolution of a spherical diapir, assuming that heat is transferred into the diapir only by conduction. We assume that the diapir is initially homogeneous in temperature at the point in which it separates from the slab. Heating of the diapir is then modeled by assuming the mantle wedge to be an infinite thermal reservoir whose initial temperature is set at 1400 °C. We assume that the initial temperature of the diapir is 700 °C, which is the temperature at which the sediments or serpentinites dehydrate and subsequently increase in viscosity so that diapiric flow – rather than channel flow – is permitted (see above for discussion on this transition). Fig. 8a shows how a diapir with a 10 km radius heats up. In this calculation, the ambient mantle is fixed at 1400 °C at a distance much greater than the diffusive length scale. Fig. 8b shows how the centers of diapirs of different radii evolve in temperature. Large diapirs, of course, heat up more slowly. Assuming that the buoyant material making up the diapir has already been dehydrated, we compare these temperature curves to the dry granite solidus temperature (~1200 °C at 2 GPa) to evaluate if melting will occur.

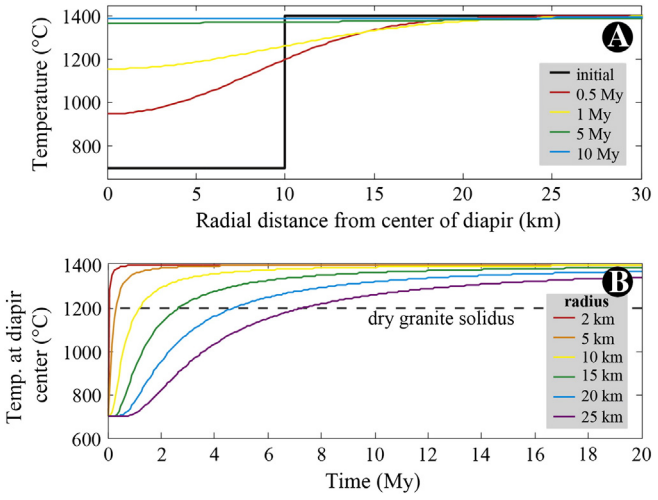

Fig. 8. (A) Cross-sectional 1-D temperature profiles achieved after 0.5, 1, 5, and 10 My of heat diffusion into a radially symmetric diapir at 700 °C with a radius of 10 km. Thick black line shows the initial conditions. The host is fixed to 1400 °C at a significant distance from the diapir margin. (B) 1-D heat diffusion profiles through time at the center of a diapir, for various diapir radii. Dashed line corresponds to the dry granite solidus at 2.0 GPa.

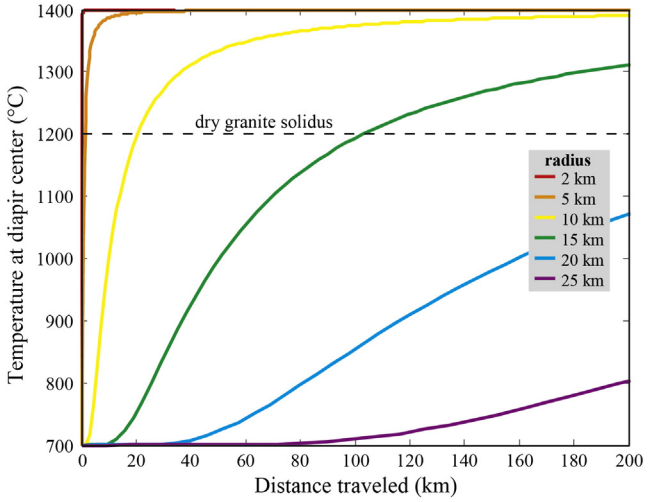

Fig. 9. Temperature at the center of a diapir versus vertical distance traveled at Stokes settling velocity, for various radii. Dashed line corresponds to the dry granite solidus at 2.0 GPa.

To determine whether a diapir would melt before relaminating to the base of the over-riding plate, we estimate the vertical distance a diapir will travel by the time it melts. This is done by multiplying the time for melting by the diapir ascent velocity (Fig. 9). We note that the retention of partial melts in a diapir would decrease its bulk density, thereby increasing its buoyancy, so these traveling distances are minimum bounds. Although the timescales of heating small diapirs are much faster than large diapirs, the ascent rates of small diapirs are far slower than large diapirs (i.e. Stokes' law; Fig. 5). This means that diapirs that are too large will not melt. Diapirs that are too small will rise slowly and thus will melt, but these slowly rising diapirs may become entrained within the mantle flow field, preventing relamination or exhumation. Our calculations suggest that diapirs with a radius < 10 km will melt before traveling 20 km vertically. If small diapirs do form and separate from the slab, these results suggest that the melting diapirs could contribute to arc lavas, as suggested by Behn et al. (2011), or they may be entrained in the mantle flow field. Our calculations also suggest that large-radius diapirs will melt only partially and may remain largely intact during their ascent through the mantle. We recognize that deflection due to corner flow, internal deformation and melting, chemical exchange with the mantle, petrologic evolution, and barriers to flow (such as viscosity and density heterogeneities or ponding at the base of the crust) complicates the exhumation of buoyant material. The possible importance of some of these processes is discussed by Behn et al. (2011), Gerya and Meilick (2011), Hacker et al. (2011), and Marschall and Schumacher (2012).

5. Conclusions

Recent papers have drawn attention to exhumation in subduction zones (e.g. Behn et al., 2011; Hacker et al., 2011, 2013; Kylander-Clark et al., 2012; Marschall and Schumacher, 2012), raising questions about the mechanics, exhumation paths, and likely consequences of rising buoyant material. With implications for the chemical evolution of the crust through time, transport of material through subduction zones, and the composition of volcanic arcs, the fate of subducted material is an important chemical and physical consideration on Earth. This study explores the implications and limitations of buoyancy-driven exhumation of high-pressure, low-temperature terranes in the following ways.

1. We compiled 45 high-pressure, low-temperature terranes worldwide for which robust thermobarometry exists, categorizing each according to its tectonic environment and protolith. We show that oceanic-type terranes form under pressures less than ~2.7 GPa whereas continental-types form under greater pressures and along slightly higher geothermal gradients.
2. We propose a buoyancy-driven model to explain the separation of the two end-member terrane types in P–T space, suggesting that channel flow operates at shallow pressures to exhume oceanic-type terranes whereas continental-type terranes ascend via diapirism following slab dehydration. Balancing buoyancy forces and viscous drag, we determine the velocities of channel flow and diapiric ascent to depend on the density difference between the buoyant material and mantle wedge, gravitational acceleration, channel thickness squared, and inversely on viscosity. Channel flow velocity additionally depends on slab dip.
3. We predict where the transition between exhumation modes occurs along the slab–mantle interface by calculating when dehydration occurs. For simplicity, we model dehydration to be temperature-dependent rather than vary with composition. Modeling dehydration to coincide with heat diffusion reaching 700 °C, we find that the timescales of dehydration depend on the initial thermal state of the slab, channel thickness, and inversely on heat diffusivity. The transition from channel flow to diapirism depends on slab dip and the viscosity contrast between the subducted buoyant material and the overlying mantle wedge. We predict that the dominant mode of exhumation varies along the slab–mantle interface as well as during the closure of an ocean basin according to changes in these two parameters.
4. We model the fate of rising diapirs by determining whether or not they will melt. Modeling heat diffusion into rising diapirs, we find that those with radii less than 10 km will melt during the ascent through the mantle, where they may contribute to arc volcanism or be entrained in the mantle flow field. Larger diapirs may partially melt but remain largely intact during their ascent, suggesting that they may relaminate to the base of the crust and potentially exhume to the surface.

In summary, our model provides a simple, but predictive, framework for understanding the transport of chemically buoyant material in subduction zones.

Supplementary data to this article can be found online at http://dx.doi.org/10.1016/j.earscirev.2014.08.012.

Acknowledgments

We thank Y. Niu and W. G. Ernst for their insightful reviews of the manuscript. This study benefitted from helpful discussions with R. Dasgupta and A. Lenardic. M. Erdman additionally thanks ExTerra (a sub-division of the NSF's GeoPRISMS program) for providing an inviting forum in which to discuss our ideas. This research was supported by the NSF (EAR-1347085).

References

Bakun-Czubarow, N., 1991. On the possibility of occurrence of quartz pseudomorphs after coesite in the eclogite–granulite rock series of the Zlote Mountains in the Sudetes (SW Poland). Arch. Mineral. 47, 5–16.
Bakun-Czubarow, N., 1992. Quartz pseudomorphs after coesite and quartz exsolution in eclogitic omphacites of the Zlote Mountains in the Sudetes (SW Poland). Arch. Mineral. 48, 3–25.
Baldwin, S.L., Webb, L.E., Monteleone, B.D., 2008. Late Miocene coesite–eclogite exhumed in the Woodlark Rift. Geology 36, 735.
Ballèvre, M., Pitra, P., Bohn, M., 2003. Lawsonite growth in the epidote blueschists from the Ile de Groix (Armorican Massif, France): a potential geobarometer. J. Metamorph. Geol. 21, 723–735.
Bally, A.W., 1981. Thoughts on the tectonics of folded belts. Thrust and Nappe Tectonics. Geological Society, London, Special Publications, pp. 13–32.
Bauer, C., Rubatto, D., Krenn, K., Proyer, A., Hoinkes, G., 2007. A zircon study from the Rhodope metamorphic complex, N-Greece: time record of a multistage evolution. Lithos 99, 207–228.
Beaumont, C., Jamieson, R.A., Butler, J.P., Warren, C.J., 2009. Crustal structure: a key constraint on the mechanism of ultra-high-pressure rock exhumation. Earth Planet. Sci. Lett. 287, 116–129.

Behn, M.D., Kelemen, P.B., Hirth, G., Hacker, B.R., Massonne, H.-J., 2011. Diapirs as the source of the sediment signature in arc lavas. Nat. Geosci. 4, 641–646.

Bills, B.G., Currey, D.R., Marshall, G.A., 1993. Viscosity estimates for the crust and upper mantle from patterns of lacustrine shoreline deformation in the Eastern Great Basin. J. Geophys. Res. 99, 22,059–22,086.

Bosse, V., Féraud, G., Ballèvre, M., Peucat, J.-J., Corsini, M., 2005. Rb–Sr and $^{40}Ar/^{39}Ar$ ages in blueschists from the Ile de Groix (Armorican Massif, France): implications for closure mechanisms in isotopic systems. Chem. Geol. 220, 21–45.

Bostick, B.C., Jones, R.E., Ernst, W.G., Chen, C., Leech, M.L., Beane, R.J., 2003. Low-temperature microdiamond aggregates in the Maksyutov Metamorphic Complex, South Ural Mountains, Russia. Am. Mineral. 88, 1709–1717.

Brey, G.P., Köhler, T., 1990. Geothermobarometry in four-phase lherzolites II. New thermobarometers, and practical assessment of existing thermobarometers. J. Petrol. 31, 1353–1378.

Bröcker, M., Fotoohi Rad, G.R., Burgess, R., Theunissen, S., Paderin, I., Rodionov, N., Salimi, Z., 2013. New age constraints for the geodynamic evolution of the Sistan Suture Zone, eastern Iran. Lithos 170–171, 17–34.

Bromiley, G.D., Pawley, A.R., 2003. The stability of antigorite in the systems $MgO–SiO_2–H_2O$ (MSH) and $MgO–Al_2O_3–SiO_2–H_2O$ (MASH): the effects of Al^{3+} substitution on high-pressure stability. Am. Mineral. 88, 99–108.

Brown, M., 2007. Metamorphic conditions in orogenic belts: a record of secular change. Int. Geol. Rev. 49, 193–234.

Burov, E., Jolivet, L., Le Pourhiet, L., Poliakov, A., 2001. A thermomechanical model of exhumation of high pressure (HP) and ultra-high pressure (UHP) metamorphic rocks in Alpine-type collision belts. Tectonophysics 342, 113–136.

Caby, R., 1994. Precambrian coesite from northern Mali: first record and implications for plate tectonics in the trans-Saharan segment of the Pan-African belt. Eur. J. Mineral. 6, 235–244.

Carlson, R.L., 2001. Chapter 13: rock and Earth's crust. In: Levy, M., Bass, H.E., R.R.S. (Eds.), Handbook of Elastic Properties of Solids, Liquids, and Gases. Academic Press, pp. 377–461.

Caron, J.-M., Péquignot, G., 1986. The transition between blueschist and lawsonite-bearing eclogites based on observations from Corsican metabasalts. Lithos 19, 205–218.

Chemenda, A.I., Mattauer, M., Malavieille, J., Bokun, A.N., 1995. A mechanism for syn-collisional rock exhumation and associated normal faulting: results from physical modelling. Earth Planet. Sci. Lett. 132, 225–232.

Chopin, C., 1984. Coesite and pure pyrope in high-grade blueschists of the Western Alps: a first record and some consequences. Contrib. Mineral. Petrol. 86, 107–118.

Clarke, G.L., Aitchison, J.C., Cluzel, D., 1997. Eclogites and blueschists of the Pam Peninsula, NE New Caledonia: a reappraisal. J. Petrol. 38, 843–876.

Clift, P., Vannucchi, P., 2004. Controls on tectonic accretion versus erosion in subduction zones: implications for the origin and recycling of the continental crust. Rev. Geophys. 42, RG2001.

Cloos, M., 1982. Flow melanges: numerical modeling and geologic constraints on their origin in the Franciscan subduction complex, California. Geol. Soc. Am. Bull. 93, 330–345.

Coleman, R.G., Lee, D.E., 1963. Glaucophane-bearing metamorphic rock types of the Cazadero Area, California. J. Petrol. 4, 260–301.

Conrad, C.P., Molnar, P., 1997. The growth of Rayleigh–Taylor-type instabilities in the lithosphere for various rheological and density structures. Geophys. J. Int. 129, 95–112.

Corfu, F., Krogh-Ravna, E.J., Kullerud, K., 2003. A Late Ordovician U–Pb age for the Tromsø Nappe eclogites, Uppermost Allochthon of the Scandinavian Caledonides. Contrib. Mineral. Petrol. 145, 502–513.

Currie, C.A., Beaumont, C., Huismans, R.S., 2007. The fate of subducted sediments: a case for backarc intrusion and underplating. Geology 35, 1111.

Cuthbert, S.J., Carswell, D.A., Krogh-Ravna, E.J., Wain, A., 2000. Eclogites and eclogites in the Western Gneiss Region, Norwegian Caledonides. Lithos 52, 165–195.

Ellis, D.J., Green, D.H., 1979. An experimental study of the effect of Ca upon garnet–clinopyroxene Fe–Mg exchange equilibria. Contrib. Mineral. Petrol. 71, 13–22.

Endo, S., Wallis, S., Hirata, T., Anczkiewicz, R., Platt, J., Thirlwall, M., Asahara, Y., 2009. Age and early metamorphic history of the Sanbagawa belt: Lu–Hf and P–T constraints from the Western Iratsu eclogite. J. Metamorph. Geol. 27, 371–384.

Ernst, W.G., 1975. Systematics of large-scale tectonics and age progressions in Alpine and Circum-Pacific blueschist belts. Tectonophysics 26, 229–246.

Ernst, W.G., 1993. Metamorphism of Franciscan tectonostratigraphic assemblage, Pacheco Pass area, east-central Diable Range, California Coast Ranges. Geol. Soc. Am. Bull. 105 (5), 618–636.

Ernst, W.G., 2005. Alpine and Pacific styles of Phanerozoic mountain building: subduction-zone petrogenesis of continental crust. Terra Nova 17, 165–188.

Ernst, W.G., Maruyama, S., Wallis, S., 1997. Buoyancy-driven, rapid exhumation of ultrahigh-pressure metamorphosed continental crust. Proc. Natl. Acad. Sci. U. S. A. 94, 9532–9537.

Fitzherbert, J.A., 2003. Lawsonite–omphacite-bearing metabasites of the Pam Peninsula, NE New Caledonia: evidence for disrupted blueschist- to eclogite-facies conditions. J. Petrol. 44, 1805–1831.

Fotoohi Rad, G.R., Droop, G.T.R., Amini, S., Moazzen, M., 2005. Eclogites and blueschists of the Sistan Suture Zone, eastern Iran: a comparison of P–T histories from a subduction mélange. Lithos 84, 1–24.

Gerya, T.V., Meilick, F.I., 2011. Geodynamic regimes of subduction under an active margin: effects of rheological weakening by fluids and melts. J. Metamorph. Geol. 29, 7–31.

Gerya, T.V., Stöckhert, B., Perchuk, A.L., 2002. Exhumation of high-pressure metamorphic rocks in a subduction channel: a numerical simulation. Tectonics 21 (6–1–6–19).

Gerya, T.V., Connolly, J.A.D., Yuen, D.A., Gorczyk, W., Capel, A.M., 2006. Seismic implications of mantle wedge plumes. Phys. Earth Planet. Inter. 156, 59–74.

Ghent, E.D., Stout, M.Z., Erdmer, P., 1993. Pressure–temperature evolution of lawsonite-bearing eclogites, Pinchi Lake, British Columbia. J. Metamorph. Geol. 11, 279–290.

Ghent, E.D., Tinkham, D., Marr, R., 2009. Lawsonite eclogites from the Pinchi Lake area, British Columbia—new P–T estimates and interpretation. Lithos 109, 248–253.

Gilotti, J.A., Krogh-Ravna, E.J., 2002. First evidence for ultrahigh-pressure metamorphism in the North-East Greenland Caledonides. Geology 30, 551–554.

Green, T.H., Hellman, P.L., 1982. Fe–Mg partitioning between coexisting garnet and phengite at high pressure, and comments on a garnet–phengite geothermometer. Lithos 15, 253–266.

Groppo, C., Castelli, D., 2010. Prograde P–T evolution of a lawsonite eclogite from the Monviso Meta-ophiolite (western Alps): dehydration and redox reactions during subduction of oceanic FeTi-oxide gabbro. J. Petrol. 51 (12), 2489–2514.

Guillot, S., Hattori, K.H., de Sigoyer, J., Nägler, T., Auzende, A.-L., 2001. Evidence of hydration of the mantle wedge and its role in the exhumation of eclogites. Earth Planet. Sci. Lett. 193, 115–127.

Guiraud, M., Holland, T.J.B., Powell, R., 1990. Calculated mineral equilibria in the greenschist–blueschist–eclogite facies in $Na_2O–FeO–MgO–Al_2O_3–SiO_2–H_2O$. Contrib. Mineral. Petrol. 104, 85–98.

Hacker, B.R., 2006. Pressures and temperatures of ultrahigh-pressure metamorphism: implications for UHP tectonics and H_2O in subducting slabs. Int. Geol. Rev. 48, 1053–1066.

Hacker, B.R., Abers, G.A., Peacock, S.M., 2003. Subduction factory 1. Theoretical mineralogy, densities, seismic wave speeds, and H_2O contents. J. Geophys. Res. 108, 2029.

Hacker, B.R., Kelemen, P.B., Behn, M.D., 2011. Differentiation of the continental crust by relamination. Earth Planet. Sci. Lett. 307, 501–516.

Hacker, B.R., Gerya, T.V., Gilotti, J.A., 2013. Formation and exhumation of ultrahigh-pressure terranes. Elements 9, 289–293.

Hall, P.S., Kincaid, C., 2001. Diapiric flow at subduction zones: a recipe for rapid transport. Science 292, 2472–2475 (80-.).

Harley, S.L., 1984. An experimental study of the partitioning of Fe and Mg between garnet and orthopyroxene. Contrib. Mineral. Petrol. 86, 359–373.

Harley, S.L., Green, D.H., 1982. Garnet–orthopyroxene barometry for granulites and peridotites. Nature 300, 697–701.

Harlow, G.E., Hemming, S.R., Avé Lallemant, H.G., Sisson, V.B., Sorensen, S.S., 2004. Two high-pressure–low-temperature serpentinite-matrix mélange belts, Motagua fault zone, Guatemala: a record of Aptian and Maastrichtian collisions. Geology 32, 17.

Hermann, J., 2003. Experimental evidence for diamond-facies metamorphism in the Dora-Maira massif. Lithos 70, 163–182.

Heuret, A., Conrad, C.P., Funiciello, F., Lallemand, S., Sandri, L., 2012. Relation between subduction megathrust earthquakes, trench sediment thickness and upper plate strain. Geophys. Res. Lett. 39, L05304.

Hill, E.J., Baldwin, S.L., Lister, G.S., 1995. Magmatism as an essential driving force for formation of active metamorphic core complexes in eastern Papua New Guinea. J. Geophys. Res. 100, 10441.

Hirajima, T., Banno, S., Hiroi, Y., Ohta, Y., 1988. Phase petrology of eclogites and related rocks from the Motalafjella high-pressure metamorphic complex in Spitsbergen (Arctic Ocean) and its significance. Lithos 22, 75–97.

Hirth, G., Kohlstedt, D.L., 1996. Water in the oceanic upper mantle: implications for rheology, melt extraction and the evolution of the lithosphere. Earth Planet. Sci. Lett. 144, 93–108.

Hirth, G., Kohlstedt, D.L., 2003. Rheology of the upper mantle and the mantle wedge: a view from the experimentalists. In: Eiler, J. (Ed.), Inside the Subduction Factory. Geophysical Monograph American Geophysical Union, Washington, D.C., pp. 83–105.

Holland, T.J.B., 1979. Experimental determination of the reaction paragonite = jadeite + kyanite + H_2O, and internally consistent thermodynamic data for part of the system $Na_2O–Al_2O_3–SiO_2–H_2O$, with applications to eclogites and blueschists. Contrib. Mineral. Petrol. 301, 293–301.

Holland, T.J.B., 1980. The reaction albite = jadeite + quartz determined experimentally in the range 600–1200 degrees C. Am. Mineral. 65, 129–134.

Horodyskyj, U., Lee, C.-T.A., Luffi, P., 2009. Geochemical evidence for exhumation of eclogite via serpentinite channels in ocean–continent subduction zones. Geosphere 5, 426–438.

Hoschek, G., 2001. Thermobarometry of metasediments and metabasites from the Eclogite zone of the Hohe Tauern, Eastern Alps, Austria. Lithos 59, 127–150.

Hoschek, G., 2007. Metamorphic peak conditions of eclogites in the Tauern Window, Eastern Alps, Austria: thermobarometry of the assemblage garnet + omphacite + phengite + kyanite + quartz. Lithos 93, 1–16.

Huang, W.L., Wyllie, P.J., 1973. Melting relations of muscovite–granite to 35 kbar as a model for fusion of metamorphosed subducted oceanic sediments. Contrib. Mineral. Petrol. 42, 1–14.

Jahn, B., Caby, R., Monie, P., 2001. The oldest UHP eclogites of the World: age of UHP metamorphism, nature of protoliths and tectonic implications. Chem. Geol. 178, 143–158.

Janák, M., Froitzheim, N., Lupták, B., Vrabec, M., Ravna, E.J.K., 2004. First evidence for ultrahigh-pressure metamorphism of eclogites in Pohorje, Slovenia: tracing deep continental subduction in the Eastern Alps. Tectonics 23 (n/a–n/a).

Krogh-Ravna, E.J., 2000. The garnet–clinopyroxene Fe^{2+}–Mg geothermometer: an updated calibration. J. Metamorph. Geol. 18, 211–219.

Krogh-Ravna, E.J., Terry, M.P., 2004. Geothermobarometry of UHP and HP eclogites and schists—an evaluation of equilibria among garnet–clinopyroxene–kyanite–phengite–coesite/quartz. J. Metamorph. Geol. 22, 579–592.

Krogh-Ravna, E.J., Oh, C.W., Liou, J.G., 1994. Polyphase and anticlockwise P–T evolution for Franciscan eclogites and blueschists from Jenner, California, USA. J. Metamorph. Geol. 12, 121–134.

Kylander-Clark, A.R.C., Hacker, B.R., Mattinson, J.M., 2008. Slow exhumation of UHP terranes: titanite and rutile ages of the Western Gneiss Region, Norway. Earth Planet. Sci. Lett. 272, 531–540.
Kylander-Clark, A.R.C., Hacker, B.R., Mattinson, C.G., 2012. Size and exhumation rate of ultrahigh-pressure terranes linked to orogenic stage. Earth Planet. Sci. Lett. 321–322, 115–120.
Lardeaux, J.M., Ledru, P., Daniel, I., Duchene, S., 2001. The Variscan French Massif Central—a new addition to the ultra-high pressure metamorphic "club": exhumation processes and geodynamic consequences. Tectonophysics 332, 143–167.
Liou, J.G., Hacker, B.R., Zhang, R.Y., 2000. Into the forbidden zone. Science 287, 4–6 (80-.).
Liou, J.G., Tsujimori, T., Zhang, R.Y., Katayama, I., Maruyama, S., 2004. Global UHP metamorphism and continental subduction/collision: the Himalayan model. Int. Geol. Rev. 46, 1–27.
Little, T.A., Hacker, B.R., Gordon, S.M., Baldwin, S.L., Fitzgerald, P.G., Ellis, S., Korchinski, M., 2011. Diapiric exhumation of Earth's youngest (UHP) eclogites in the gneiss domes of the D'Entrecasteaux Islands, Papua New Guinea. Tectonophysics 510, 39–68.
Lü, Z., Zhang, L., Du, J., Bucher, K., 2008. Coesite inclusions in garnet from eclogitic rocks in western Tianshan, northwest China: convincing proof of UHP metamorphism. Am. Mineral. 93, 1845–2008.
Marschall, H.R., Schumacher, J.C., 2012. Arc magmas sourced from mélange diapirs in subduction zones. Nat. Geosci. 5, 862–867.
Maruyama, S., Liou, J.G., Terabayashi, M., 1996. Blueschists and eclogites of the world and their exhumation. Int. Geol. Rev. 38, 485–594.
Massonne, H.-J., 1999. A new occurrence of microdiamond in quartzo-feldspathic rocks of the Saxonian Erzgebirge, Germany, and their metamorphic evolution. In: Gurney, J.J., Gurney, L.G., Pascoe, M.D., Richardson, S.H. (Eds.), Proceedings of the 7th International Kimberlite Conference. Cape Town. Redroof Publishing, Cape Town, South Africa, pp. 533–539.
Massonne, H.-J., Schreyer, W., 1989. Stability field of the high-pressure assemblage, talc + phengite and two new phengite barometers. Eur. J. Mineral. 1, 391–410.
Mattinson, C.G., Wooden, J.L., Liou, J.G., Bird, D.K., Wu, C.L., 2006. Age and duration of eclogite-facies metamorphism, North Qaidam HP/UHP terrane, Western China. Am. J. Sci. 306, 683–711.
Mitrovica, J.X., 1996. Haskell [1935] revisited. J. Geophys. Res. 101, 555–569.
Mposkos, E.D., Kostopoulos, D.K., 2001. Diamond, former coesite and supersilicic garnet in metasedimentary rocks from the Greek Rhodope: a new ultrahigh-pressure metamorphic province established. Earth Planet. Sci. Lett. 192, 497–506.
Mukherjee, B.K., Sachan, H.K., 2001. Discovery of coesite from Indian Himalaya: a record of ultra-high pressure metamorphism in Indian continental crust. Curr. Sci. 81, 1358–1361.
Nakamura, D., Svojtka, M., Naemura, K., Hirajima, T., 2004. Very high-pressure (>4 GPa) eclogite associated with the Moldanubian Zone garnet peridotite (Nové Dvory, Czech Republic). J. Metamorph. Geol. 22, 593–603.
O'Brien, P.J., Zotov, N., Law, R., Khan, M.A., Jan, M.Q., 2001. Coesite in Himalayan eclogite and implications for models of India–Asia collision. Geology 29, 435–438.
Och, D.J., Leitch, E.C., Caprarelli, G., Watanabe, T., 2003. Blueschist and eclogite in tectonic melange, Port Macquarie, New South Wales, Australia. Mineral. Mag. 67, 609–624.
Okay, A.I., Harris, N.B.W., Kelley, S.P., 1998. Exhumation of blueschists along a Tethyan suture in northwest Turkey. Tectonophysics 285, 275–299.
Palmeri, R., Talarico, F.M., Ricci, C.A., 2011. Ultrahigh-pressure metamorphism at the Lanterman Range (northern Victoria Land, Antarctica). Geol. J. 46, 126–136.
Parkinson, C.D., Miyazaki, K., Wakita, K., Barber, A.J., Carswell, D.A., 1998. An overview and tectonic synthesis of the pre-Tertiary very-high-pressure metamorphic and associated rocks of Java, Sulawesi and Kalimantan, Indonesia. Isl. Arc 7, 184–200.
Parkinson, C.D., Motoki, A., Onishi, C.T., Maruyama, S., 2001. Ultrahigh-pressure pyrope-kyanite granulites and associated eclogites in Neoproterozoic nappes of Southeast Brazil. UHPM Workshop. Waseda University, pp. 87–90.
Perraki, M., Proyer, A., Mposkos, E.D., Kaindl, R., Hoinkes, G., 2006. Raman microspectroscopy on diamond, graphite and other carbon polymorphs from the ultrahigh-pressure metamorphic Kimi Complex of the Rhodope Metamorphic Province, NE Greece. Earth Planet. Sci. Lett. 241, 672–685.
Platt, J.P., 1993. Exhumation of high-pressure rocks: a review of concepts and processes. Terra Nova 5, 119–133.
Raimbourg, H., Jolivet, L., Leroy, Y., 2007. Consequences of progressive eclogitization on crustal exhumation, a mechanical study. Geophys. J. Int. 168, 379–401.
Reinecke, T., 1991. Very-high pressure metamorphism and uplift of coesite bearing metasediments from the Zermatt–Saas zone, Western Alps. Eur. J. Mineral. 3, 7–17.
Rudnick, R.L., Gao, S., 2003. Composition of the continental crust. In: Holland, H.D., Turekian, K.K. (Eds.), Treatise on Geochemistry. Elsevier-Pergamon, Oxford, pp. 1–64.
Săbău, G., 2000. A possible UHP-eclogite in the Leaota Mts. (South Carpathians) and its history from high-pressure melting to retrograde inclusion in a subduction melange. Lithos 52, 253–276.
Saleeby, J., 2003. Segmentation of the Laramide Slab—evidence from the southern Sierra Nevada region. Geol. Soc. Am. Bull. 115, 655–668.
Schmädicke, E., Will, T.M., 2003. Pressure-temperature evolution of blueschist facies rocks from Sifnos, Greece, and implications for the exhumation of high-pressure rocks in the Central Aegean. J. Metamorph. Geol. 21, 799–811.
Schmidt, M.W., Poli, S., 1998. Experimentally based water budgets for dehydrating slabs and consequences for arc magma generation. Earth Planet. Sci. Lett. 163, 361–379.
Schmidt, M.W., Vielzeuf, D., Auzanneau, E., 2004. Melting and dissolution of subducting crust at high pressures: the key role of white mica. Earth Planet. Sci. Lett. 228, 65–84.
Schmidt, S., Nagel, T.J., Froitzheim, N., 2010. A new occurrence of microdiamond-bearing metamorphic rocks, SW Rhodopes, Greece. Eur. J. Mineral. 22, 189–198.
Schulte, B., Sindern, S., 2002. K-rich fluid metasomatism at high-pressure metamorphic conditions: lawsonite decomposition in rodingitized ultramafite of the Maksyutovo Complex, Southern Urals (Russia). J. Metamorph. Geol. 20, 529–541.
Shatsky, V.S., Sobolev, N.V., Vavilov, M.A., 1995. Diamond-bearing metamorphic rocks of the Kokchetav Massif (Northern Kazakhstan). In: Coleman, R.G., Wang, X. (Eds.), Ultrahigh Pressure Metamorphism. Cambridge University Press, Cambridge, UK, pp. 427–455.
Shibakusa, H., Maekawa, H., 1997. Lawsonite-bearing eclogitic metabasites in the Cazadero area, northern California. Mineral. Petrol. 61, 163–180.
Shreve, R.L., Cloos, M., 1986. Dynamics of sediment subduction, melange formation, and prism accretion. J. Geophys. Res. 91, 10229.
Sobolev, N.V., Shatsky, V.S., 1990. Diamond inclusions in garnets from metamorphic rocks: a new environment for diamond formation. Nature 343, 742–746.
Song, S., Yang, J., Liou, J.G., Wu, C., Shi, R., Xu, Z., 2003. Petrology, geochemistry and isotopic ages of eclogites from the Dulan UHPM Terrane, the North Qaidam, NW China. Lithos 70, 195–211.
Song, S., Zhang, L., Niu, Y., Su, L., Song, B., Liu, D., 2006. Evolution from oceanic subduction to continental collision: a case study from the northern Tibetan Plateau based on geochemical and geochronological data. J. Petrol. 47 (3), 435–455.
Song, S., Zhang, L., Niu, Y., Wei, C., Liou, J., Shu, G., 2007. Eclogite and carpholite-bearing metasedimentary rocks in the North Qilian suture zone, NW China: implications for Early Paleozoic cold oceanic subduction and water transport into mantle. J. Metamorph. Geol. 25, 547–563.
Song, S., Niu, Y., Su, L., Wei, C., Zhang, L., 2014. Adakitic (tonalitic–trondhjemitic) magmas resulting from eclogite decompression and dehydration melting during exhumation in response to continental collision. Geochim. Cosmochim. Acta 130, 42–62.
Syracuse, E.M., van Keken, P.E., Abers, G.A., 2010. The global range of subduction zone thermal models. Phys. Earth Planet. Inter. 183, 73–90.
Tagiri, M., Yano, T., Bakirov, A., Yakajima, T., Uchiumi, S., 1995. Mineral parageneses and metamorphic P–T paths of ultrahigh-pressure eclogites from Kyrgyzstan Tien-Shan. Isl. Arc 4, 280–292.
Tsuchiya, S., Hirajima, T., 2013. Evidence of the lawsonite eclogite facies metamorphism from an epidote-glaucophane eclogite in the Kotsu area of the Sanbagawa belt, Japan. J. Mineral. Petrol. Sci. 108, 166–171.
Tsujimori, T., Ernst, W.G., 2014. Lawsonite blueschists and lawsonite eclogites as proxies for palaeo-subduction zone processes: a review. J. Metamorph. Geol. 32, 437–454.
Tsujimori, T., Sisson, V.B., Liou, J.G., Harlow, G.E., Sorensen, S.S., 2006. Very-low-temperature record of the subduction process: a review of worldwide lawsonite eclogites. Lithos 92, 609–624.
Turcotte, D.L., Schubert, G., 2002. Geodynamics, 2nd ed. Cambridge University Press, New York.
Vielzeuf, D., Schmidt, M.W., 2001. Melting relations in hydrous systems revisited: application to metapelites, metagreywackes and metabasalts. Contrib. Mineral. Petrol. 141, 251–267.
Wada, I., Wang, K., 2009. Common depth of slab–mantle decoupling: reconciling diversity and uniformity of subduction zones. Geochem. Geophys. Geosyst. 10.
Wang, X., Liou, J.G., Mao, H.K., 1989. Coesite-bearing eclogite from the Dabie Mountains in central China. Geology 17, 1085–1088.
Warren, C.J., Beaumont, C., Jamieson, R.A., 2008. Formation and exhumation of ultra-high-pressure rocks during continental collision: role of detachment in the subduction channel. Geochem. Geophys. Geosyst. 9.
Waters, D.J., 1996. The garnet–cpx–phengite barometer—recommended calibration and calculation method, (URL http://www.earth.ox.ac.uk/~davewa/research/eclogites/ecbarcal.html accessed 3.20.14).
Waters, D.J., Martin, H.N., 1993. Geobarometry of phengite-bearing eclogites. Terra Abstracts 5, 410–411.
Watson, E.B., Harrison, T.M., 2005. Zircon thermometer reveals minimum melting conditions on earliest Earth. Science 308, 841–844.
Watson, E.B., Wark, D.A., Thomas, J.B., 2006. Crystallization thermometers for zircon and rutile. Contrib. Mineral. Petrol. 151, 413–433.
Zack, T., Moraes, R., Kronz, A., 2004a. Temperature dependence of Zr in rutile: empirical calibration of a rutile thermometer. Contrib. Mineral. Petrol. 148, 471–488.
Zack, T., Rivers, T., Brumm, R., Kronz, A., 2004b. Cold subduction of oceanic crust: implications from a lawsonite eclogite from the Dominican Republic. Eur. J. Mineral. 16, 909–916.
Zhang, R.Y., Hirajima, T., Banno, S., Cong, B., Liou, J.G., 1995. Petrology of ultrahigh-pressure rocks from the southern Su–Lu region, eastern China. J. Metamorph. Geol. 13, 659–675.
Zhang, J., Zhang, Z., Xu, Z., Yang, J., Cui, J., 2001. Petrology and geochronology of eclogites from the western segment of the Altyn Tagh, northwestern China. Lithos 56, 187–206.
Zhang, L., Ai, Y., Li, X., Rubatto, D., Song, B., Williams, S., Song, S., Ellis, D., Liou, J.G., 2007. Triassic collision of western Tianshan orogenic belt, China: evidence from SHRIMP U–Pb dating of zircon from HP/UHP eclogitic rocks. Lithos 96, 266–280.
Zhang, G., Ellis, D.J., Christy, A.G., Zhang, L., Niu, Y., Song, S., 2009. UHP metamorphic evolution of coesite-bearing eclogite from the Yuka terrane, North Qaidam UHPM belt, NW China. Eur. J. Mineral. 21, 1287–1300.
Zhang, R.Y., Liou, J.G., Omori, S., Sobolev, N.V., Shatsky, V.S., Iizuka, Y., Lo, C.-H., Ogasawara, Y., 2012. Tale of the Kulet eclogite from the Kokchetav Massive, Kazakhstan: initial tectonic setting and transition from amphibolite to eclogite. J. Metamorph. Geol. 30, 537–559.